universität wien

MASTERARBEIT / MASTER'S THESIS

Titel der Masterarbeit / Title of the Master's Thesis

"CORRELATION BETWEEN GAS AND STARS IN YOUNG PROTO-CLUSTERS"

verfasst von / submitted by

Thomas Neuhauser, BSc

angestrebter akademischer Grad / in partial fulfillment of the requirements for the degree of

Master of Science (MSc)

Wien, 2022 / Vienna 2022

Studienkennzahl lt. Studienblatt / degree programme code as it appears on the student record sheet:	A 066 861
Studienrichtung lt. Studienblatt / degree programme as it appears on the student record sheet:	Astronomie
Betreut von / Supervisor:	Ass.-Prof. Dr. Alvaro Hacar Gonzalez

Acknowledgements

I thank all those who made it possible for me to walk this special path and who walked it with me as far as it was possible for them. Special thanks to my beloved wife Kati, who spent countless hours sharing her husband with astrophysics.

I would also want to thank Professor Hacar for his patience and helpful remarks, which were crucial to the successful completion of my project.

Contents

Abstract

Dense pockets of gas collapse under gravity in molecular clouds, giving rise to sun-like stars. In order to understand the star formation process, it is essential to examine the interactions between these stars and their parental gas, as it can provide insight into the timescale of evolution and accretion, as well as the global and local gas efficiencies and the distribution of newborn stars.

This project will investigate the relationship between young stellar populations and dense gas in five clusters in the Orion molecular cloud complex, LDN1641 N, OMC 4 and OMC 3 in Orion A and NGC 2023 and NGC 2024 in Orion B. The study is based on IRAM 30 m N_2H^+(1-0) molecular line observations for tracing the dense gas and on the Catalogue of Point Sources and YSOs (Megeath et al., 2012).

One finding of the research is, that in the majority of the locations studied, dense gas structures have been formed and have also been depleted multiple times during the lifespan of the oldest of the examined stellar population. Furthermore the investigated parameters like Star Formation Rate and Star Formation Efficiency shows a heterogeneous picture within the five regions, as well as the correlation between the different star populations and the dense gas component. In order to bring out more clearly the multiple conditions responsible for the heterogeneous picture, additional influencing components such as magnetic fields, gravitational and turbulence influences as well as radiation at these locations should be included in the analyses.

Zusammenfassung

In Molekülwolken kollabieren dichte Gasansammlungen unter dem Einfluss der Schwerkraft und lassen Sterne entstehen, die unserer Sonne ähnlich sind. Um den Prozess der Sternentstehung zu verstehen, ist es wichtig, die Wechselwirkungen zwischen diesen jungen Sternen und dem sie umgebenden Gas zu untersuchen, da diese Aufschluss über die Zeitskala für die Entwicklung und Akkretion sowie über die globale und lokale Gaseffizienz und die Verteilung der Sterne geben kann.

In diesem Projekt wird die Beziehung zwischen den jungen Sternpopulationen und dichtem Gas in fünf Regionen im Orion Komplex untersucht: LDN1641 N, OMC 4 und OMC 3 in der Orion A Molekülwolke, sowie NGC 2023 und NGC 2024 in der Orion B Molekülwolke. Das Datenmaterial basiert auf Beobachtungen von N_2H^+(1-0) Molekülllinien mit dem IRAM 30 m Radioteleskop zum Nachweis der Gaskomponente mit hoher Dichte und auf dem Catalogue of Point Sources and YSOs (Megeath et al., 2012).

Ein Ergebnis der Arbeit ist, dass für die Mehrzahl der untersuchten Gebiete, die dichten Gasstrukturen bereits mehrfach gebildet wurden und auch wieder aufgelöst worden sind, während der Lebensdauer der ältesten der untersuchten Sternpopulationen. Die untersuchten Parameter wie z.B. Sternentstehungsrate und Sternentstehungseffizienz zeigen ein heterogenes Bild innerhalb der fünf Regionen, ebenso die Korrelation zwischen den verschiedenen Sternpopulationen und der Komponente an Gas hoher Dichte. Um die unterschiedlichen Bedingungen, die für das heterogene Bild verantwortlich sind, genauer zu bestimmen, sollten weitere Einflussfaktoren wie Magnetfelder, gravitative und turbulente Einflüsse sowie die Strahlung in diesen Gebieten in die Untersuchungen miteinbezogen werden.

List of Tables

List of Figures

Chapter 1

Introduction

The interaction between parental gas and the Young Stellar Object (YSO) resulting from it is essential to the understanding of the formation of sun-like stars. It has been proposed that star formation occurs in the high gas density region within molecular clouds (E. A. Lada, 1992). The molecular clouds show partly hierarchical structures. One approach to characterize this structure is to assume the cloud is composed of subunits, referred as clumps and defined as coherent regions in position-velocity space, that may contain substructures as cores being defined as gravitationally bound, single peaked regions out of which stars or stellar systems can form (Williams et al., 2000). Another approach to characterize the cloud structure assumes that the cloud is self-similar, imprinted in its internal filamentarity, where star-forming cores are associated with filaments (see Hacar et al., 2022, for a review).

In Figure 1.1 the hierarchical structure from clouds to stars is presented. These cores form through the concentration of over dense regions within turbulent, filamentary molecular clouds. During the gravitational collapse, stars can form in these cores (Shu et al., 1987). One puzzle in understanding how stars form in clusters is the source of mass. Is all of the mass in place before the first stars are born, or is there an extended period when the cluster accretes material which can continuously fuel the star formation process (Kirk et al., 2013)?

Additional a fuller understanding of star formation must involve the alternation of gas between low and high density phases. A YSO, at the beginning of his devel-

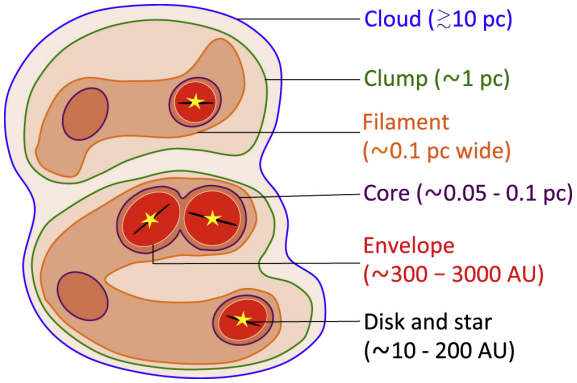

Figure 1.1: A cartoon display of a molecular cloud showing hierarchical structures inside the cloud. The figure shows the cloud, clumps, filaments, cores, envelopes and protostellar systems. Adapted from Pokhrel et al. (2018).

opment path, still accreting from its natal envelope can be examined to determine the gas density that contributed to the formation of these protostars by probing the density of this gas. More advanced YSOs may leave their original area of formation or disperse the gas. Therefore, observations of gas in the present era area not representative of the gas that produced these further evolved stars (Burkert & Hartmann, 2013). In other words, is there a cycle of formation, dispersion and repeated formation of dense star-forming gas?

The analysis of the relationship between the dense component of the molecular gas and the developmental stage of the YSOs is the content of this work.

In the following Sections of this Chapter, an introduction to the Interstellar Medium and Molecular Clouds is given in Section 1.1, the Tracer Molecule N_2H^+ in Section 1.2, Pre and Protostellar Cores in Section 1.3, Young Stellar Objects in Section 1.4 and Orion in Section 1.5. Section 1.6 outlines Previous Results.

The other Chapters cover Observations and Data in Chapter 2, Methods used in Chapter 3, Results and Discussions in Chapter 4 and the Conclusion in Chapter 5.

1.1 The Interstellar Medium and Molecular Clouds

The region between the stars is called the Interstellar Medium (ISM). It is made up of gas and dust grains. The ISM is inhomogeneous with temperatures from 10

K to 10^6 K. The densities range from 10^{-4} cm^{-3} to 10^8 cm^{-3} (Shu et al., 1987). The molecular clouds discussed above are the cold and dark places of the ISM composed of molecular gas, which can be studied with molecular-line observations, where it is observed that it consists mostly of molecular hydrogen (H_2) (Weinreb et al., 1963).

An important question is how the molecular gas is formed, which is fundamentally important for star formation. The formation of dense gas is probably not monolithic, but the result of different regions collapsing at different times. So we have different evolved star forming regions, one is older and contains evolved YSOs, one is just starting to form YSOs, and one is just starting to form dense gas but does not yet form stars (Burkert and Hartmann, 2013).

Another important question on the path to star formation is how exactly the gas collapses into individual cores. This question is still being debated.

Another concern is the life span of molecular clouds. Studies in Orion demonstrate that star clusters with ages more than 4 Myr have mostly lost their primordial gas (e.g. Dolan and Mathieu, 2001). Not only do molecular clouds form stars rapidly, but they are also transient structures that dissipate shortly, once star formation begins. The energy input from massive stars stellar winds, or more easily from Supernova (SN) shocks, appears to be able to account for gas dispersal on short timescales in both high density regions typical of molecular cloud complexes and low-density regions. If enough star energy is injected into the gas to reduce the column density by a factor of 2-3, the H_2 self-shielding may be reduced sufficiently to allow dissociation of much of the gas into the atomic phase, essentially "dissipating" the molecular cloud (Briceño et al., 2007).

1.2 Tracer Molecule N_2H^+

The most abundant molecule in molecular clouds H_2, does not emit strongly under most cloud conditions, yet it cannot be used as a direct tracer of these clouds. Different key tracers can be used to study differenPre and Protostellar Cores t gas properties in molecular clouds, allowing for a more targeted analysis. N-bearing molecules such as N_2H^+ are inhibited in their formation in diffuse gas. The only

reaction producing N_2H^+ is the protonation of N_2. N_2H^+ only survives in regions where the electron abundance is low (to prevent dissociative recombination).

After the CO freeze-out onto dust grains at temperatures < 20 K and densities $n(H_2) \geq 10^4$ cm^{-3} the abundance of N_2H^+ molecules rapidly increases. The N_2H^+ integrated emission linearly increases with the total column density of gas traced in the continuum (Caselli et al., 2002). Therefore, it can be concluded that N_2H^+ can be used as an indicator for the cold and dense regions within a cloud, which selectively highlights the star-forming material (e.g. Bergin and Tafalla, 2007; Pety et al., 2017; Hacar, Tafalla, and Alves, 2017).

1.3 Pre and Protostellar Cores

There are two types of cores, separated in pre-stellar and protostellar. The pre-stellar core is a gravitationally bound core that is stabilized against collapse by thermal, turbulent, and magnetic pressure (Shu et al., 1987; Andre et al., 2000; di Francesco et al., 2007; Ward-Thompson et al., 2007). Protostellar cores are gravitationally collapsing cores containing protostars. In order to cause gravitational collapse to form a star, several mechanisms have been proposed: Ambipolar diffusion, dissipation of turbulent support, and external triggers like mass inflow (Shu et al., 1987; Bonnell et al., 1997). Prestellar cores can collapse gravitationally, forming protostars. A pre-stellar core that is gravitationally collapsing can keep its low temperature and continue collapsing because radiation can escape and radiate away the energy.

As the collapse proceeds, the central density increases, leading to increasing opacity for radiation. Due to this increasing opacity in the pre-stellar core, radiation is trapped in the centre, leading to the formation of an initial hydrostatic core. Since the radiation can no longer escape, this leads to an increasing temperature and an adiabatic contraction of the core (the resulting heat is completely converted into internal energy of the gas). During this, gas from the surrounding medium still falls gravitationally onto the central core. This leads to an accretion shock that either radiates the incident energy away or deposits this energy in the adiabatic core. As the process progresses, the temperature rises until it reaches 2000 K. As a result,

the molecular hydrogen dissociates. Due to the endothermic nature of this process, the first core collapses quickly as the internal support is removed. Once all H_2 is dissociated, the gravitational collapse is stopped again, leading to the formation of a second, much more compact core (Larson, 1969). This second core continues its adiabatic contraction while the surrounding gas falls on the core. At this moment we speak of a protostellar core, whose further development leads to the early YSOs.

1.4 Young Stellar Objects

YSOs are a class of stars in their early stages of formation, characterized by strong emission from gas and dust. They result from the fragmentation of structures such as filaments and fibres and the processes discussed in section 1.3.

For the understanding of the formation and evolution of YSOs, the collection and classification of physical quantities are necessary. For the evolved stars the Hertzsprung-Russel diagram is used to classify groups of stars by their luminosity, the total amount of energy radiated by a star per second, and effective temperature T_{eff}, the photospheric temperature of the star (Hertzsprung, 1905; Russell, 1914). This classification scheme cannot be applied to the early phase of stellar evolution, because the YSO does not have a well defined photosphere, radiating as a blackbody at a constant temperature T_{eff}. The spectrum of an YSO, in his early evolutionary stage, is caused by the components gas and dust, with a wide range of temperature, which results in a much broader spectrum than a blackbody (Beichman et al., 1986).

YSOs are described in one of the classification schemes with quantities other than temperature, based on the slope of their spectral energy distribution (SED) in the infrared, α_{IR}, from 2 to $\sim$20 μm. This slope is used to measure the distribution of luminous flux as a function of wavelength (C. J. Lada & Wilking, 1984). Figure 1.2 is showing some of the SEDs of the first studied protostar cluster in Rho Ophiuchi.

Another classification characteristic is their bolometric temperature T_{bol}, as a measure of the circumstellar obscuration and evolutionary development. T_{bol} is the temperature of a blackbody having the same mean frequency as the observed continuum spectrum (Myers & Ladd, 1993).

Together with the discovery of the Class 0 by Andre et al. (1993), Greene et al. (1994) identified 5 classes of YSOs:

Class 0, no α_{2-14}, high $L_{\mathrm{sub-mm}}/\ L_{\mathrm{bol}}$.

Class I, $\alpha_{2-14} > 0.3$, $T_{\mathrm{bol}} < 650$ K.

Flat Spectrum, -0.3 $< \alpha_{2-14} <$ 0.3, $T_{\mathrm{bol}} \sim$ 400-800 K.

Class II, -2 $< \alpha_{2-14} <$ -0.3, 650 $< T_{\mathrm{bol}} <$ 2800 K.

Class III, $\alpha_{2-14} <$ -2, $T_{\mathrm{bol}} >$ 2800 K.

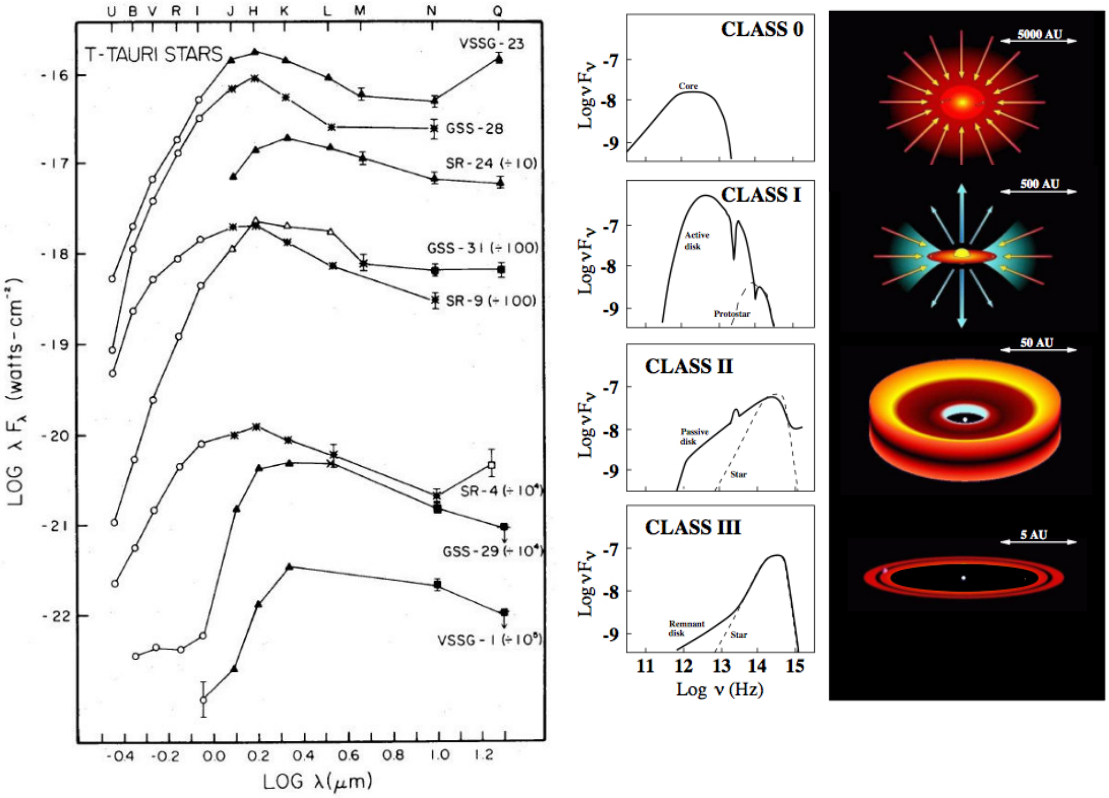

Figure 1.2: Left: Energy distribution for YSOs in the core of Rho Ophiuchi (C. J. Lada & Wilking, 1984). **Right:** This diagram illustrates the evolution of YSOs (Andrea Isella 2006). The left column shows a typical SED for each class, the right column shows a cartoon of its geometry. In addition, Class Flat should be mentioned, which lies between Class I and Class II. The name originates from the flat shape of the SED in the transition from Class I to Class II.

Class 0 YSOs are the youngest objects, with a spectral energy distribution that is dominated by the sub-millimetre and far-infrared regimes. They are usually embedded in dense envelopes of molecular gas and dust and may still be in the collapse stage. Their single peaked SEDs are blackbody curves that include the protostellar radiation re-emitted by the gas and dust envelope.

The conservation of angular momentum prevents the circumstellar envelope from collapsing directly onto the protostar. A torus-like structure forms, which evolves into a circumstellar disk, from which the protostar accumulates mass and evolves further to the next class of protostars (Preibisch, 2012).

Class I objects form as soon as most of the material in the envelope has collapsed onto the disk, the central protostar becomes observable at infrared wavelengths. This moment is defined as the "birth" of the star (Palla & Stahler, 1999). Their SED curves are a combination of the stellar photosphere and the disk at this stage of evolution and are therefore upward sloping with $\alpha_{2-14} > 0.3$ and peak in the far infrared. During the accretion process, the central core of Class I objects grows and the circumstellar accretion disk begins to flatten.

Flat Spectrum stars show SED curves that are flat with -0.3 $< \alpha_{2-14} <$ 0.3. They are the transition between accreting from a thick disk Class I protostars and low accreting from thin disks Class II pre-main sequence stars.

Class II stars have a spectral energy distribution that is still dominated by the near-infrared regime. Almost all of the circumstellar material is now found in a optical thick, flattened disk of gas and dust. Their SED curves are sloping in the near-infrared, but in this range they are still clearly above the black body curve of the young star with a slope of between -2 $< \alpha_{2-14} <$ -0.3. The infrared excess starts at about 2 μm. The peak of the SED in this phase of development comes from the blackbody curve of the star. These pre-main sequence stars can be detected in the optical, depending on the inclination of the surrounding disk. Accretion at this stage produces strong emission lines, especially the Hα emission line, typical for Classical T-Tauri Stars. One possible explanation for Hα emission is that material from the accretion disk falls onto the stellar surface, creating a hot spot from where the emission lines originate.

Class III objects show an SED that resembles a stellar photosphere, with low emission from the, made up of dust and planitesimals, so called debris disk (C. J. Lada et al., 2006; Preibisch, 2012). The infrared excess through the disk is seen at wavelengths from 10 to 20 μm. The slope of the SED is $\alpha_{2-14} <$ -2. Class III stars already have observable photospheres very similar to those of a main sequence star, with ages of 7-10 Myr for low-mass stars (Briceno et al., 2007). They are also called weak-line T Tauri stars because the accretion rate at this stage is very low and emission lines are weak. At constant mass, they evolve towards the Zero-Age Main Sequence in the Hertzsprung-Russel diagram. An overview of the classes and their corresponding SEDs is given in Figure 1.2.

1.5 Orion

On a clear winter night in the Northern Hemisphere, the constellation Orion can be seen moving across the night sky. One part of this constellation is the Orion molecular cloud (OMC). The OMC, which produces low and high mass stars, is the closest (about 400 pc) and best characterised giant molecular cloud (GMC) complex. It has a multitude of various star formation environments. The structures observed in Orion are shaped by several physical mechanisms like gravitational collapse, thermal, turbulent and magnetic pressure, angular momentum and dynamical feedback from young stellar outflows, winds and radiation pressure (e.g. Takahashi et al., 2013 , Contreras et al., 2016, Teixeira et al., 2016).

It is home to the GMCs Orion A and Orion B, from which many theories have been and are being derived, e.g. on star formation and knowledge about YSOs, cloud structure and OB associations. OB associations are clusters of hot massive stars in the spectral classes O and B. Orion A and B provide the opportunity to study star formation in a single cloud complex over a range of environments, from regions directly impacted by massive star formation, over moderate sized clusters, to very quiet regions with mostly isolated star formation (Stanke et al., 2022).

The Orion-Eridanus super-bubble, also known as Orion's Cloak, surrounds Orion A and B and is partially visible by Hα emission in the east, which is known as

Barnard's Loop, as shown in Figure 1.3. The region is thought to have been formed in the last 12 million years by 30 to 100 massive stars ($> 8M_{\odot}$), of which up to 20 of the more massive ones ended in SN explosions (Bally, 2008). This SN explosion released high kinetic energies, resulting in a large bubble of X-ray emitting gas.

The four age-related subgroups (OB1a/b/c/d) of the Orion OB1 association are partially superimposed along the line-of-sight (Blaauw, 1964). The OB1a subgroup is thought to be the oldest, dating back 8 to 12 Myr and located approximately 350 pc away (Blaauw, 1991; Brown et al., 1994; Bally, 2008). It is located north-west of the belt, near δ Orionis (Mintaka), and stretches almost as far as or γ Orionis (Bellatrix), though Bellatrix is not counted among the members of the Orion complex.

The OB1b subgroup is estimated to be between 2-8 Myr old at a distance of about 400 pc and is located around the belt stars that are members of this subgroup and it overlaps with the southern parts of the Orion B GMC.

The subcluster σ Orionis is rather assigned to the subgroup OB1c due to its age of 2-3 Myr (Walter et al., 2008). σ Orionis is a system of five luminous stars with spectral types ranging from A to O, located near the Horsehead Nebula. With an age of 2 to 6 Myr, the OB1c subgroup is partly located south of the eastern belt-star ζ Orionis (Alnitak) and in front of and south of the Orion Nebula Cluster (ONC). It is superimposed on the subgroups OB1b and OB1d, with an estimated distance of 400 pc (Bally, 2008). Because of its similar age, the λ Orionis cluster is sometimes associated with the OB1c sub-clusters as a detached portion.

It is possible that the older members of OB1a triggered the formation of both the northern λ Orionis group and the southern OB1c group (Bally, 2008). OB1c also contains stars in the upper part of Orion's Sword with the bright clusters NGC 1977 and NGC 1981, as well as stars in front and below the ONC that mostly belong to NGC 1980, including ι Orionis.

NGC 1977 is an open cluster of about 100 young stars that form a reflection and emission line nebula north of the Orion Nebula and are linked to OMC 2 and 3 in the south.

The true membership of the two loose clusters NGC 1980 and 1981 is under debate. They are either older stars formed by Orion A or a completely unique

clustering. They are superimposed on parts of the younger OB1d subgroup, and it is assumed that its components are at least 10 pc in front of Orion A due to the lack of any illumination and reflection nebulae on Orion A's surface associated with members of this cluster (Bally, 2008).

The ONC belongs to the OB1d sub-group, which is the youngest of the OB1 assiciations and is located in front of the Orion A molecular cloud. This sub-group also includes NGC 2024 in Orion B and the Horsehead Nebula. Its age is given as only up to 2 Myr (Palla and Stahler, 1999). The ONC is probably the best known star cluster in the entire constellation, which also includes the famous Trapezium stars, whose four brightest components, Orionis A, B, C and D, roughly form a trapezoid. Their spectral types range from B1 to O4 whereby each is also a multiple star. It is thought that star formation in the ONC began roughly 10 Myr ago, initially at a lesser pace and subsequently steadily accelerated. The most active formation is confined to a few million years, and has recently ended with gas dispersal from the Trapezium (Palla and Stahler, 1999).

1.5.1 Orion A

The Orion A Giant Molecular Cloud is located about 19 degrees below the galactic plane. This means that the background is less affected than typically along the galactic plane. Due to the relative distance of 400 to 420 pc from Earth, it can be observed with good resolution even with a radio telescope of modest size. Its young stars and gas provide important clues about the physics of star formation, the formation, evolution and destruction of star forming clouds, the dynamics and energetics of the interstellar medium.

The Orion A region contains the Orion Nebula HII region (M42), which was formed by the stars of the ONC, including the Trapezium, as well as the HII region M43, the bright nebula and cluster NGC 1977, the star clusters NGC 1980 and NGC 1981, the Orion Molecular Clouds 1 to 5, the low-mass star forming region Lynds 1641, and the reflection nebula NGC 1999.

Orion A is cometary in appearance with a compact ridge of dense gas at the northern end, a massive filament, the integral shaped filament (ISF) (Bally et al.,

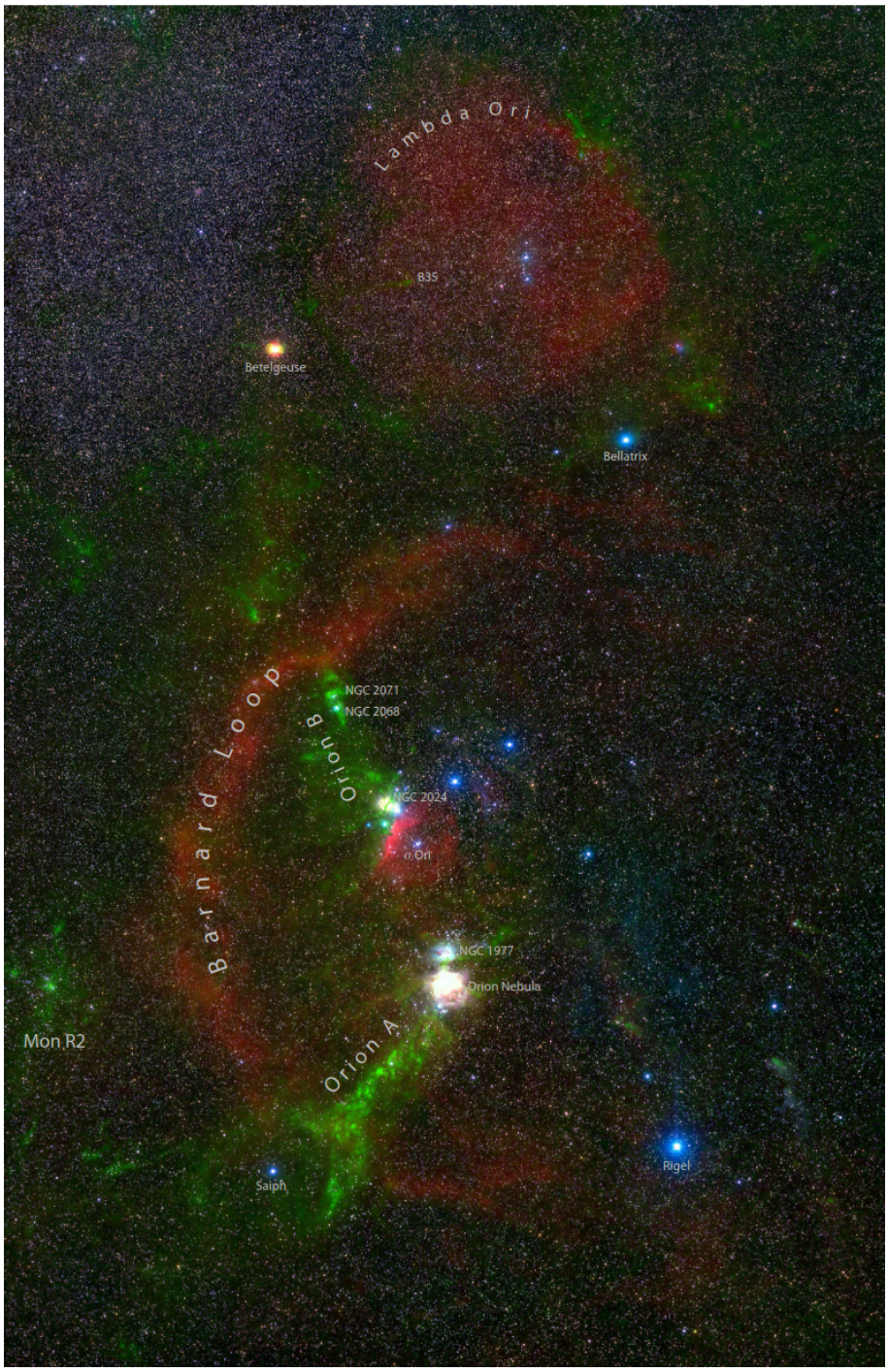

Figure 1.3: Overview of the Orion Complex. The HII regions are shown in red, the H_2 molecular clouds in green. The image is an overlay of an optical image (Wei-Hao Wang, IfA, University of Hawaii) and a dust extinction map (Lombardi et al., 2011).

1987). The ISF is among the best-studied massive filaments and is taken as a reference for theories on the formation of star clusters. The length of the ISF is more than 7 pc (Johnstone & Bally, 1999). There are identified velocity-coherent substructures called fibers. These fibers, possibly the fundamental dense components of filaments, can explain the complex substructure of the ISF as well as its current distribution of cores and protostars. Their transonic non-thermal velocity dispersions with respect to their local temperature, seems to reflect the preferred gas organization prior to the formation of stars. It is suggested that fibers are internally oriented following the local gravitational potential within the ISF. Fibers could be a fundamental and universal building block in star formation, with the observed differences in both high-mass and low-mass clouds, as well as in isolated and clustered regimes, arising from the initial concentration of fibers (Hacar et al., 2018). The ISF is usually divided into four regions known as Orion molecular clouds 1, 2, 3 and 4, which extend from north to south for about 10 pc. In the literature, the southernmost region of OMC 4 is also referred to as OMC 5.

OMC 1 is located behind the Trapezium, OMC 4 is a v-shaped cluster of submillimeter cores located south of OMC 1 (O'Dell et al., 2008). The OMC 2 and 3 region to the north contains one of the richest concentrations of protostars where vigorous star formation is active, and the cores of OMC 3 are well associated with YSOs (e.g.Jin et al., 2001). The OMC 2/3 and NGC 1977 regions are surrounded by a number of B stars, particular to the north of NGC 1977 and the east of OMC 2/3 (Peterson and Megeath, 2008). An overview of the region can be seen in Figure 1.4.

In the southern part of Orion A, a lower density and wider tail can be observed (Bally, 2008). LDN1641, the dark part of the southern cloud as seen from Earth, leads south to the ONC. It is divided into North, Center and South and runs parallel to the galactic plane for about 3 to 4 degrees from north-west to south-east beneath Orion's Sword. The two so-called "eastern" and "western legs" of the cloud, LDN1648 and LDN1647, are located at the southern end of LDN1641. Orion A has a probable distance gradient from north to south of around 100 pc, implying that LDN1641 is further distant than the ONC. (e.g. Wilson et al., 2005; Großschedl et al., 2018). LDN1641 lacks the rich clusters of the ONC region, but it does have mul-

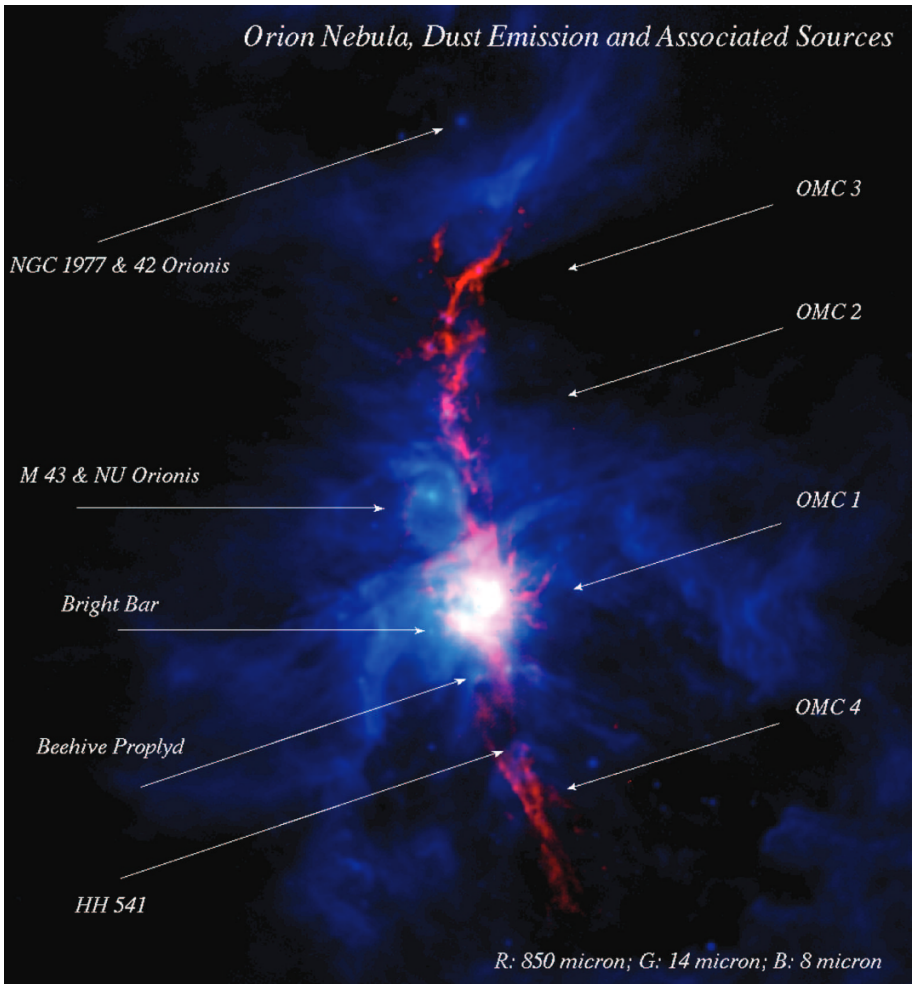

Figure 1.4: Dust map of the Orion A Molecular Cloud. The ISF and OMC 1/2/3/4 can be seen. Adopted from O'Dell et al., 2008.

tiple minor clusterings and relatively isolated YSOs, as well as about eight separate small groups of young stars found by optical, infrared, and X-ray surveys.

The most visible of the small aggregates in the north is the LDN1641 North (LDN1641 N) cluster. The reflection nebula NGC 1999 lies nearby, and it features a dark patch, which is sometimes interpreted as a dense foreground globule, a hole or cavity in the material generated by the V380 Ori jets that produce the reflection nebula NGC 1999 (Stanke et al., 2010).

LDN1641 Centre is located in the centre of the low density region. The luminous star V883 Ori, most likely a FU Ori type star, which is an embedded IR source that illuminates the reflection nebula IC430, is located to the west of LDN 1641 Center (Haro, 1953).

The southern part of LDN1641 contains the LDN1641 South reflection nebula. The LDN1641 South cluster does not appear to be deeply embedded and it orbits the B star HD 38023, the most massive member of LDN1641, which produces this reflection nebula (Racine, 1968).

1.5.2 Orion B

The Orion B cloud contains a high density ridge at its western end where the embedded clusters NGC 2024 and NGC 2023 and the Horsehead Nebula are located. A network of dust and CO filaments trails away from the OB association towards the east. The northern part of Orion B contains the NGC 2068 and NGC 2071 clusters that are embedded in dense cores at the southwestern ends of cometary clouds of CO emission. These clouds also trail off in a direction pointing away from the OB association (Bally, 2008). Orion B is located within the Hα shell "Barnard's Loop" and OB stellar aggregates which impact the cloud from the west with radiation and stellar winds. Orion B shows star formation mainly concentrated in a few moderate-sized clusters with young stars up to intermediate mass.

1.6 Previous Results

For the L1630 molecular cloud (it includes NGC 2024 and NGC 2023) was discovered, that star formation occurs almost solely within dense gas, with a density of $n(H_2) > 10^4$ cm^{-3}, and is strongly favoured in a few clumps ($M > 200$ $M_\odot$) where the efficient conversion of molecular gas into stars has resulted in the production of rich stellar clusters (E. A. Lada, 1992). Surprisingly their result showed that not all of the dense gas is actively in the star forming process. The vast majority of the stars were formed in three most massive clumps in the cloud, among them also NGC 2024. Two massive clumps show relatively low star formation activity, including as well NGC 2023. If they reflect the final star formation efficiencies (see chapter 3.8), high gas densities and high gas mass may be necessary but not sufficient for the formation of star clusters.

Gutermuth et al. (2011) found for most clouds they considered in their work a trend of decreasing Class II to Class I ratio with increasing gas column density. This may suggest that the higher column density regions are younger than those with low column density and that the YSOs at low column densities may have migrated from high density regions or may be the result of gas dispersal.

In the constellation Perseus, for the NGC 1333 proto cluster, only the young YSO's Classes 0 and I do exhibit a strong correlation with respect to the dense gas emission, traced by the N_2H^+ intensity, observed with the IRAM 30 meter telescope. (Hacar, Tafalla, & Alves, 2017). This tracer can be used to selectively study gas properties at densities of $n(H_2) \gtrsim 10^4$ cm^{-3} and temperatures $\lesssim 20$ K.

Chapter 2

Observations and Data

In the following sections, the regions covered in this work are presented in Section 2.1, as well as the observations with the IRAM 30 meter telescope to obtain the N_2H^+ data in Section 2.2. The catalogue of the YSOs detected in the Orion A and B clouds used in this work is presented in Section 2.3.

2.1 Regions

The regions under survey are inside the Orion A and B molecular clouds. Within Orion A the LDN1641 N dark cloud and the regions OMC 3 and OMC 4 were studied. The nebulae NGC 2023 and NGC 2024 were examined in Orion B. They are all part of the greater Orion Molecular Cloud Complex. In the following sections, the respective region and its immediate surroundings are discussed in more detail.

2.1.1 LDN1641 N

As LDN1641 contains no rich clusters comparable to the ONC, it is forming stars in multiple dense molecular cores found primarily along a ridge of gas that extends the length of the cloud. Most of the protostars are clustered in small groups, but the more evolved YSOs appear to be located both in and around these aggregates. LDN1641 has thus become a case study for the relative importance of "distributed" vs. "clustered" star formation. Results from the Spitzer Space Telescope survey of LDN1641 confirms the existence of a significant distributed population, in which

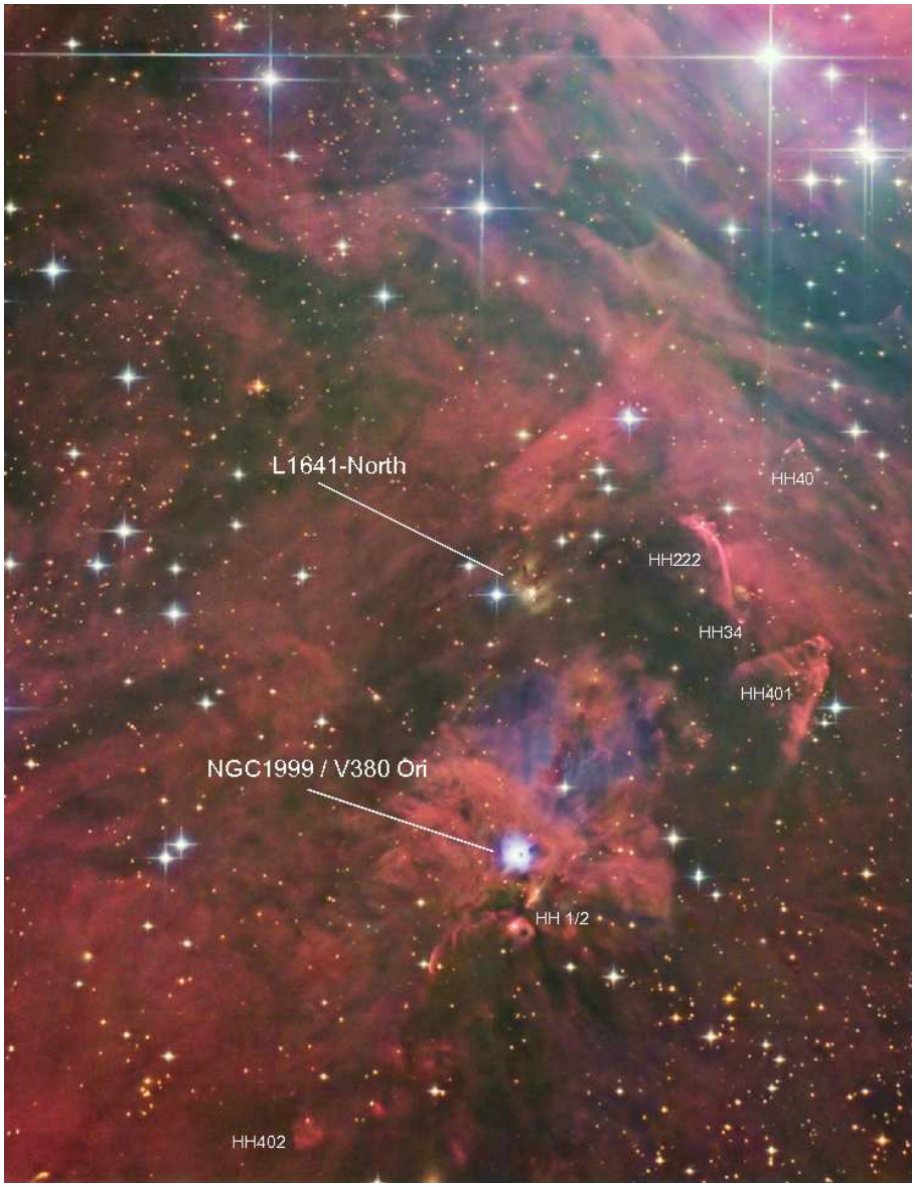

Figure 2.1: The Northern part of L 1641 molecular cloud is seen in this image composed of an Hαimage combined with R, G, B, broadband filter images. North is up and east is left. Courtesy Johannes Schedler.

44% of the young stars are in low surface density regions (Allen and Davis, 2008). LDN1641 does not contain any early B type or O stars. The lack of strong ultra violet fluxes may be important for the dense gas evolution. The most prominent group of young stars within LDN1641, LDN1641 N contains numerous YSOs (Chen et al., 1993; Strom et al., 1993).

2.1.2 OMC 4

The region referred to as OMC 4 is located at the southern end of the ISF, north of LDN1641 N. It is often also referred to as OMC 5, but is rarely found in the literature, containing a loose cluster of clumps located immediately behind the star cluster NGC 1980 (Johnstone and Bally, 2006). The far ultraviolet radiation in this area is found to be weak (Ishii et al., 2019). This may be related to the current low number of protostars and the relatively low mass of dense gas.

2.1.3 OMC 3

Interestingly, the discovery of OMC 3 is not well documented in the literature. The area is generally described alongside OMC 2 as OMC 2/3. OMC 3 is located in the northern part of the ISF, further away of the ONC than OMC 2. The OMC 2/3 region encompasses a section of the Orion A molecular cloud undergoing vigorous star forming activity. One of the richest assemblages of protostars in the nearest 500 pc is seen in OMC 2/3, containing these protostars embedded in molecular filaments, surrounded by a number of B stars. The connection between these B stars and the OMC 2/3 region is currently being debated, it is plausible that they have influenced star formation in these regions by compressing, heating and/or ionizing the molecular gas. It is suggest that the filament, which includes the OMC 2/3 area, results from the interstellar medium being compressed by a superbubble driven by the Orion OB association. The region of OMC 2/3 is located in an environment without the extreme UV radiation found in the Orion Nebula and showing lower stellar densities than found in the centre of the Orion Nebula (e.g. Bally et al., 1987; Peterson and Megeath, 2008).

2.1.4 NGC 2023

Within Orion B, NGC 2023 is a bright reflection nebula south of NGC 2024 and north-east of the Horsehead nebula, illuminated by the B1.5 star HD 37903, with the bulk of the molecular cloud located behind HD 37903 and the reflection nebula (Figure 2.2). Due to the special configuration between HD 37903, a local source of ionization, and the background cloud, NGC 2023 has also been a special target to understand the nature of photo–dissociation regions (PDRs). Studies of the background molecular cloud identified several clumps of dense gas in the region, with relatively little dense gas left in the massive clump associated with NGC 2023 compared to those associated with NGC 2024. The average column densities in the NGC 2023 region are less than the densities in other areas associated with young clusters (e.g. Harvey et al., 1980; E. A. Lada et al., 1997).

2.1.5 NGC 2024

NGC 2024, shown in Figure 2.2 and 2.3, is the most active star-forming region in Orion B. This area is characterized by an extensive HII region, exited by an early B star (IRS2b), a dark lane that persists from visible to infrared wavelengths, and a ridge of cold dust and molecular gas containing protostellar objects. The cluster was found to be young $\tau < 3$ Myr. In addition to the high-mass star, hundreds of low-mass stars are identified in the cluster by near-infrared and X ray observations. Studies tracing dense gas ($> 10^5 \mathrm{cm}^{-3}$) indicated that NGC 2024 is the most structured area in Orion B and has the highest column density and star formation efficiency in the region. The associated cloud of NGC 2024, consists of two separate velocity components that are physically coupled to the HII region as indicated by their tight connection with the dark lanes and emission nebulosity. The development of late O-type stars and early B stars and the protostars was probably caused by a cloud-cloud collision between the two components (e.g. C. J. Lada and Lada, 1991; Skinner et al., 2003; Pety et al., 2017; Enokiya et al., 2021).

Figure 2.2: In the left upper corner of the picture, NGC 2024 (The Flame Nebula) is to the left of the bright star, ζOri, with the multi–color reflection nebula NGC 2023 directly below. The Horsehead Nebula is further to the southwest of NGC 2023, with σOri, the bright star toward the edge of the frame. Courtesy Johannes Schedler. Adopted from Meyer et al., 2008.

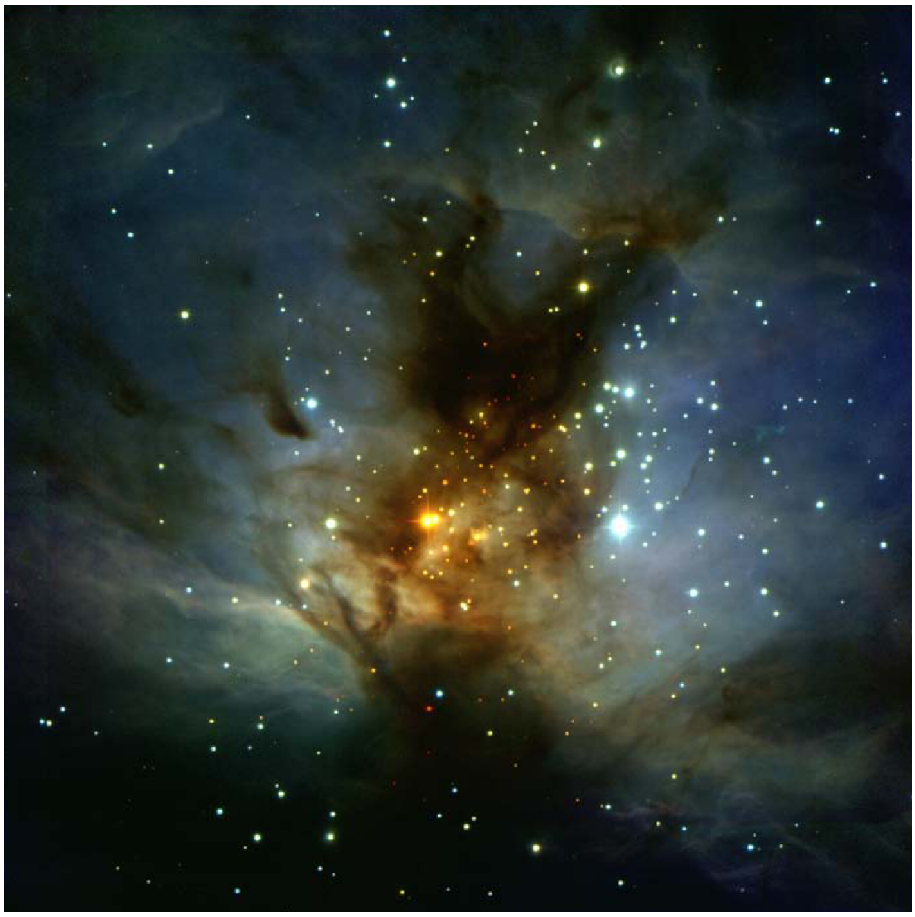

Figure 2.3: Infrared image of NGC 2024. IRS#2 can be seen as the bright red source in the heart of the visible dark lane and IRS#1 as the bright blue star to the right. Courtesy David Thompson. Adopted from Meyer et al., 2008.

2.2 IRAM

The 30 meter telescope is situated on Pico Veleta in the Spanish Sierra Nevada. It is one of today's most extensive and delicate radio telescopes for tracing millimeter waves. The telescope, a single dish parabolic antenna, is equipped with a succession of heterodyne receivers and continuum cameras that function at 3, 2, 1 and 0.9 mm. LDN1641 N, OMC 3 and OMC 4 measurements were taken in October 2020, while NGC 2024 and NGC 2023 measurements were taken in the periode from December 2020 to May 2021.

2.2.1 N_2H^+ Measurements

For the measurement of N_2H^+ intesities, IRAM measurements were carried out in a frequency range from 93.1661 to 93.1768 GHz in 550 channels. The observations were carried similar to Hacar, Alves, et al. (2017). The final maps are obtained as large mosaics combining multiple tails, typically of 200x200 arcsec^2 each, carried out in On-the-Fly, Position-Switching mode.

2.3 YSO Catalogue

To have a uniform basis for the YSOs, a catalogue is necessary that includes all the regions studied. Therefore the catalogue of Megeath et al. (2012) was used. The survey covered 8.8 deg^2 of the Orion clouds with the four IRAC bandpasses and 16.4 deg^2 with the MIPS instrument, with a combined total coverage of 8.8 deg^2. The IRAC instrument also observed eight reference fields covering 0.29 deg^2. Figure 2.4 shows the Coverage of the Spitzer Orion cloud survey. A total of 298,405 point sources are found in this field, of which 34,176 are detected in a sufficient number of wave bands that allow them to be examined for infrared excesses. This study characterized the completeness of the point source catalog as a function of magnitude across the four IRAC bands and one MIPS band.

In a given field, completeness varies spatially and is strongly dependent on nebulosity. 3479 dusty YSOs can be recognized by the fact that their emission in the

mid-infrared region exceeds what would be expected from a reddened photosphere. A total of 2991 young stars with disks are included along with 428 protostars and 50 faint candidate protostars. There are also ten other sources detected exclusively in the MIPS 24 μm band that are likely to be protostars. The identified dusty YSOs are found distributed throughout the Orion A and B molecular clouds. The YSOs are classified into the Class P for protostars and Class D for young stars with disk (Class 0, I and flat spectrum respectively Class II in the classification of Greene et al. (1994)). A distinction is also made between red candidate protostars (PR) and faint candidate protostars (FR), but these are not significant in this work, as the objects found in the catalogue query are not located within the measurement area.

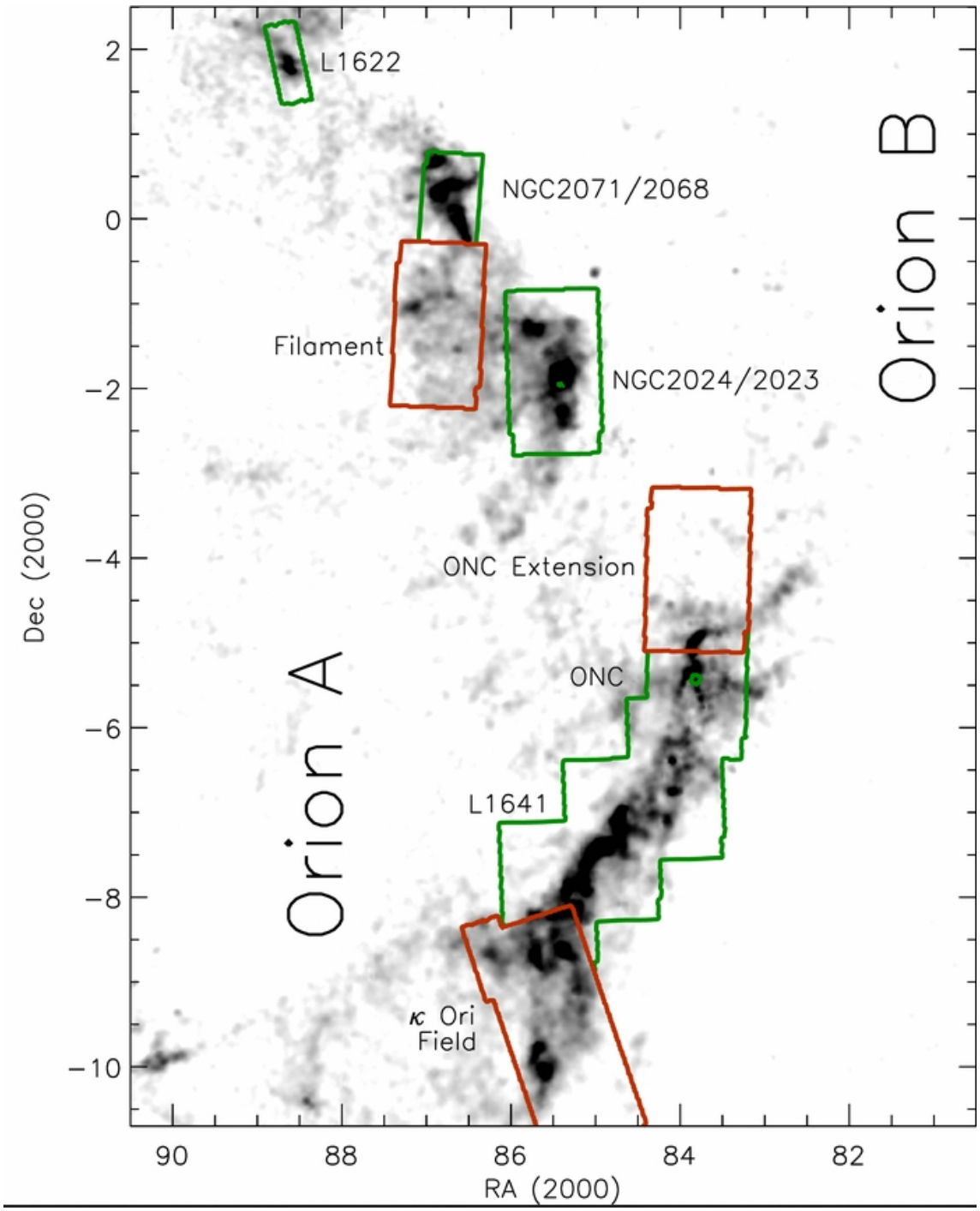

Figure 2.4: Coverage of the Spitzer Orion cloud survey. The grayscale image is an extinction map of the Orion region made from the 2MASS PSC (Gutermuth et al., 2011). Adapted from Megeath et al. (2012).

Chapter 3

Methods

The star formation process from interstellar gas raises many open questions. Among them are questions about the correlation between the position of YSOs and the dense gas component ($n(H_2) \geq 10^4$ cm^{-3}) in molecular clouds in different environments, influenced for example by massive stars and their radiation? How are the YSOs distributed in the different stages of development, are they clustered or more randomly spread? Are the YSOs of an earlier stage of development found in a different density range of the dense component of the molecular gas than those in a later stage of development?

To find the relationship between the dense gas in the form of N_2H^+ molecular line intensity measurements, which are available in the form of FITS cubes, and stars represented by YSOs, zero moment maps have been created out of the IRAM measurements for the observed regions, which in turn have been overlaid with the YSOs from the YSO catalogue (Megeath et al., 2012) to obtain a visual representation. The measured intensity values of N_2H^+ at the locations of the YSO positions have been further used to create graphs, in which the accumulated frequency of the respective YSO class has been compared to these intensities. In addition a simulation was programmed to determine the nature of the relationship between the YSO classes and the N_2H^+ intensity. The relevant regions had to be extracted from two of the five intensity measurement datasets. The programming language used is Python (Van Rossum & Drake, 2009).

To accomplish these tasks, the following four routines have been developed:

- ZEROM (Zero Moments Calculation). Section 3.2.
- FITSCUT (FITS-Cut out region of interest). Section 3.3.
- INYOUMAP (Intensity YSO Maps). Section 3.4.
- COSITOM (Compare simulated to measured distribution). Section 3.5.

The Dense Gas Mass calculation is detailed in Section 3.6, the Star Formation Rate in Section 3.7 and the Star Formation Efficiency in Section 3.8.

3.1 Program Testing

For the purpose of checking the values calculated with the programs and also the correctness of the superimposed maps from the intensity values of the N_2H^+ measurements with the positions of the YSOs, the east part of the LDN 1641 N map 3.1, which looks like a Lagotto Romagnolo 3.2, was used for comparison. The data represent N_2H^+(1-0) observations (Section 2.2). The Cube Analysis and Rendering Tool for Astronomy, CARTA v2.0 (Comrie et al., 2021), is used to view the data and generate the zero moment map, which equals the integrated intensity of the N_2H^+ (1-0) line. The YSO catalogue (Megeath et al., 2012) was queried with the VizieR catalogue access tool (Ochsenbein et al., 2000a). The resulting objects are laid over the map and the corresponding values at the positions of the YSO's are read out. This process of calculating the zero moments, superimposing the YSO catalogues and reading the intensities at the YSO positions to produce a plot is automated in the next step and the values found here are used as a reference.

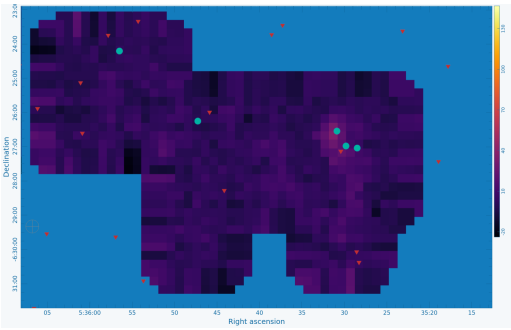

Figure 3.1: N_2H^+ zero moment map overlaid with YSO's. Protostars marked with cyan dots and pre main sequence stars marked with red triangles.

Figure 3.2: A Lagotto Romagnolo.

3.2 ZEROM Zero Moments Calculation

The given data of the observed regions in Orion, which are available in the form of FITS files, are read in successively by means of a python program. The calculation of the zero moment M_0 is done by summing the values of all measured intensities I along the spectral dimension x as shown in Eq. 3.1.

$$M_0 = \int I dx \tag{3.1}$$

The values calculated in this way were converted from [Jy km/s] to [K km/s].

The calculation is shown in Eq. 3.2,

$$Q'(\nu_0) = 1.22 \times 10^6 \left(\frac{\theta_b}{\text{arcsec}}\right)^{-2} \left(\frac{\nu_0}{\text{GHz}}\right)^{-2} [\text{K km/s per Jy km/s}], \tag{3.2}$$

where θ_b is the beam Full Width at Half Maximum (FWHM) and ν_0 is the frequenzy of the line centroid. You can find the python code used to calculate the zero moment in Appendix A.1 .

3.3 FITSCUT Cut Out Region of Interest

For data sets that contain larger areas than the region to be searched, it was necessary to restrict the data set to the area of interest. For this purpose, a routine was developed that cuts out the requested area from the existing FITS file and creates a new FITS file for further processing. The Cutout2D routine from the python package astropy (Astropy Collaboration et al., 2022) was used for this operation. The python code can be found in Appendix A.2 .

3.4 INYOUMAP Intensity YSO Maps

In order to obtain those YSOs listed in the catalogue of Megeath et al. (2012) within the areas to be investigated, a query was made using VizieR queries, a Python interface for querying astronomical web forms and databases like the VizieR web service (Ochsenbein et al., 2000b). For this purpose, the centre point coordinate of the intensity map is determined by means of the fits header. The database search was limited to an area of 20 arcseconds around the centre. This value was determined visually from the maximum size of the surveyed areas. The search was also limited to Class P and Class D objects (Section 2.3). The YSOs from the catalogue are superimposed on the zero moment map. See code in Appendix A.3.

3.5 COSITOM Compare Simulated to Measured Distribution

The mapping of the YSO Class P and Class D and the N_2H^+ intensity is cumulatively plotted in a diagram with the number of objects of the respective class within an intensity range. Furthermore, a simulation was carried out in which a random distribution on the intensity map was simulated for the Class D YSOs. For this purpose, the number of Class D YSOs was determined for each area. This number of objects was then randomly distributed on the N_2H^+ intensity map and the process was repeated 1000 times. For the Class P objects found in each region, a simulation

with quadratic weighting of the N_2H^+ intensity has been created in the same way. It was also repeated 1000 times. These results of the simulations are also shown cumulatively in the diagrams, code see Appendix A.4.

3.6 Dense Gas Mass

The calculation of the dense gas mass is done by summing up all the positive values of the intensity I(N_2H^+) within the areas mapped by the observations. With the relationship from (Hacar, Tafalla, & Alves, 2017),

$$N\ (H_2)[cm^{-2}] = \left(7.9 \cdot I\ [N_2H^+]\ [K\ km\ s^{-1}] + 8.2\right) \times 10^{21}, \tag{3.3}$$

between the observed N_2H^+ intensities and the column density N(H_2), the total amount of dense gas is derived. To note is that the completeness of the measurement is limited by the coverage of the observed areas with respect to the total extension of these areas.

3.7 The Star Formation Rate

An estimate of the Star Formation Rate (SFR) (Megeath et al., 2022) is given by

$$SFR((M_\odot Myr^{-1}) = m_\star \frac{n_{YSO}}{t_{YSO}}, \tag{3.4}$$

with n_{YSO} is the number of YSOs, t_{YSO} is the lifetime of the YSOs in Myr, and $m_\star$ is the average mass for a typical YSO ($0.5 M_\odot$). The value used for n_{YSO} in this work, is the total number of Class P and Class D objects. The combined lifetime of Class P $\approx$ 0.5 Myr and for Class D objects $\approx$ 2 Myr, 2.5 Myr can be used for t_{YSO}.

3.8 Star Formation Efficiency

As a direct and statistically robust measurement of the efficiency of gas mass converted into YSOs, the Star Formation Efficiency (SFE) (C. J. Lada & Lada, 2003) is a fundamental parameter describing the evolution of young stellar clusters. The current SFE in dense gas is given by

$$SFE = \frac{m_\star n_{YSO}}{M_{cloud} + m_\star n_{YSO}}, \tag{3.5}$$

where n_{YSO} is the number of Class P objects. M_{cloud} is the total mass detected in N_2H^+. The typical stellar mass for Class P object is assumed to be 0.5 $M_\odot$.

Chapter 4

Results and Discussions

The procedures described in Chapter 3 have been carried out for all target areas LDN1641 N, OMC 4, OMC 3, NGC 2023 and NGC 2024. When the N_2H^+ intensity maps were created, they were overlaid with the positions of the Class P objects and Class D objects. The graph produced with the cumulative frequencies of the Class P and Class D objects in relation to the measured intensities of N_2H^+ was also combined with the simulations (Section 3.5) for comparison. The calculations from the Sections 3.6 for gas mass, 3.7 for the SFR and 3.8 for the SFE are included in the results of the areas and are summarised in tabular form in Section 4.5 as the ratio of Class D objects to Class P objects, named as F_D. Furthermore, the percentage of Class P objects with values of intensity above $I(N_2H^+) > 5$ [K km s^{-1}] is included in Table 4.1, referred to as Class P_{5K}. For Class P_{5K} the threshold $I(N_2H^+) > 5$ [K km s^{-1}] was chosen to obtain values above 0% in the low intensity areas OMC 4 and NGC 2023 and for areas with high intensities, like LDN1641 N and OMC 3 to get values below 100% . The areas are discussed from south namely LDN1641 N to north i.e. NGC 2024.

4.1 ORION A

4.1.1 LDN1641 N

The generated map for LDN1641 N is shown in Figure 4.1. One can see that the Class D objects, marked with red dots, are distributed within and around the intensity areas with $I(N_2H^+) > 5$ [K kms^{-1}], enclosed by the second contour, while the Class P objects, marked with white asterisk, are highly concentrated at these intensities within the map. The value of the contour with $I(N_2H^+) = 5$ [K km s^{-1}] was chosen because it can still be displayed in areas with a lower maximum intensity such as NGC 2023 and OMC 4 and thus a comparison with the maps of LDN1641 N, OMC 3 and NGC 2024 is possible. The graph displayed below shows also the deviation from the simulated random distribution of the Class D objects. The shape of the curve tends towards the square-weighted distribution for 30% of the objects in the higher intensity part of the figure. The Class P objects show a much stronger than quadratic correlation to high intensities in the graph.

As for all the regions studied, a value for F_D is obtained, the Class D to Class P objects ratio. The ratio F_D is compared to the dense gas mass per pc^2 in section 4.4. The result found in this way is compared with that from Gutermuth et al., 2011. The value of $F_D = 3$ is in the middle range of the values found. The SFR is at ≈ 10 $M_\odot$/Myr in the lower range of the observed areas. The value for the current SFE is with 2.7% also at the low range of the studied regions. In LDN1641 N, 95% of Class P objects are at intensities above $I(N_2H^+) > 5$ [K km s^{-1}]. This high percentage value and especially the cumulative plot represent very well the situation of a young proto-cluster and its YSO populations in relation to dense gas components. The curves suggest that the cluster is embedded in the parental molecular cloud.

4.1.2 OMC 4

For OMC 4 in Figure 4.2, the map shows a random distribution of the Class D objects. This can be seen in the lower graph of Figure 4.2, by the congruent course of the curve for the random distribution and the Class D objects. For the Class P objects, a correlation with the denser regions can be seen in the map. The shape of the square-weighted randomised distribution and the observed Class P objects show a picture divided into two parts . It can be observed that 30% of the Class P objects are located in areas of lower intensity with a tendency towards a random distribution. The remaining 70% of the Class P objects is found in the region which indicates a more than quadratic relationship.

The value for $F_D = 6.4$ is the highest value found. The SFR is at $\approx 13\ M_\odot$/Myr and the current SFE is at the value of $\approx 4.5\%$. In OMC 4 the proportion is 33% of the Class P objects are found at values of $I(N_2H^+) > 5$ [K km s^{-1}]. The star formation seems to be dying down, except for smaller areas with higher gas densities.

4.1.3 OMC 3

The northernmost region of Orion A surveyed, OMC 3, shows a random distribution for the Class D objects as can be seen in Figure 4.3. This can also be seen in the shape of the graph of the Class D objects with the simulated random distribution. The two curves are nearly identical. In the map can be seen a division into two by a diagonal shape that shapes from north-east to south-west. With the exception of one YSO, the Class P objects are found in the southern part. Their local correspondence with high intensities is clearly visible in this region.

The graph shows that the correlation of the Class P objects to high intensities is higher than the quadratic shown in the simulation. The value for $F_D = 3.7$. The SFR is at $\approx 23\ M_\odot$/Myr and the SFE is at $\approx 5\%$. There are 79% of the Class P objects found at values for $I(N_2H^+) > 5$ [K km s^{-1}]. The picture here is twofold. In the northern part there is little recent star formation with fairly dense gas structures and in the southern part there is intense star formation with high gas density.

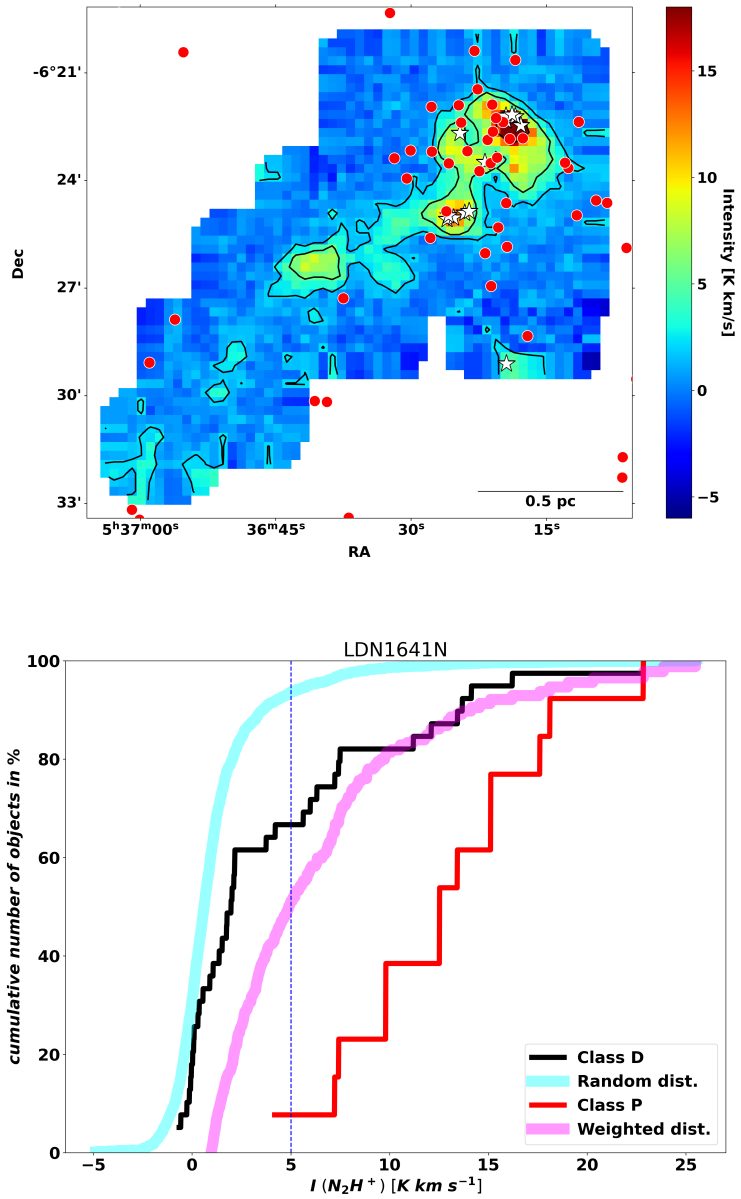

Figure 4.1: Top: *LDN1641 N* N_2H^+ intensity emission map (intensity level is colour coded in black), with positions of Class D objects (red dots) and Class P objects (white asterisk). Contour levels show 2 and 5 [K km s^{-1}] N_2H^+ intensities. **Bottom**: The cumulative number of Class D (black line) and Class P objects (red line) as a function of N_2H^+ intensity. The cyan and magenta curves correspond to the cumulative proportion of objects resulting from the simulation (see 3.5) for the random distribution and the square-weighted distribution. The vertical line corresponds to the 5 [K km s^{-1}] N_2H^+ intensity contour in the top plot.

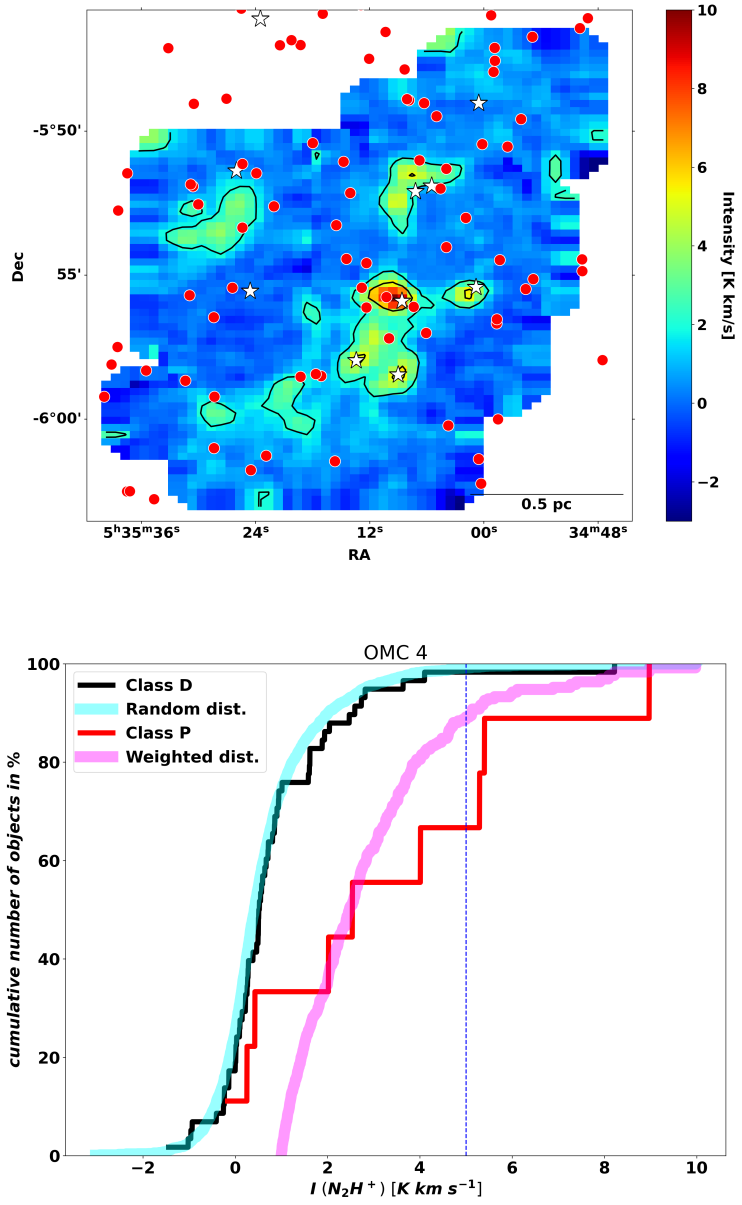

Figure 4.2: Top: *OMC 4* N_2H^+ intensity emission map (intensity level is colour coded in black), with positions of Class D objects (red dots) and Class P objects (white asterisk). Contour levels show 2 and 5 [K km s^{-1}] N_2H^+ intensities. **Bottom**: The cumulative number of Class D (black line) and Class P objects (red line) as a function of N_2H^+ intensity. The cyan and magenta curves correspond to the cumulative proportion of objects resulting from the simulation (see 3.5) for the random distribution and the square-weighted distribution. The vertical line corresponds to the 5 [K km s^{-1}] N_2H^+ intensity contour in the top plot.

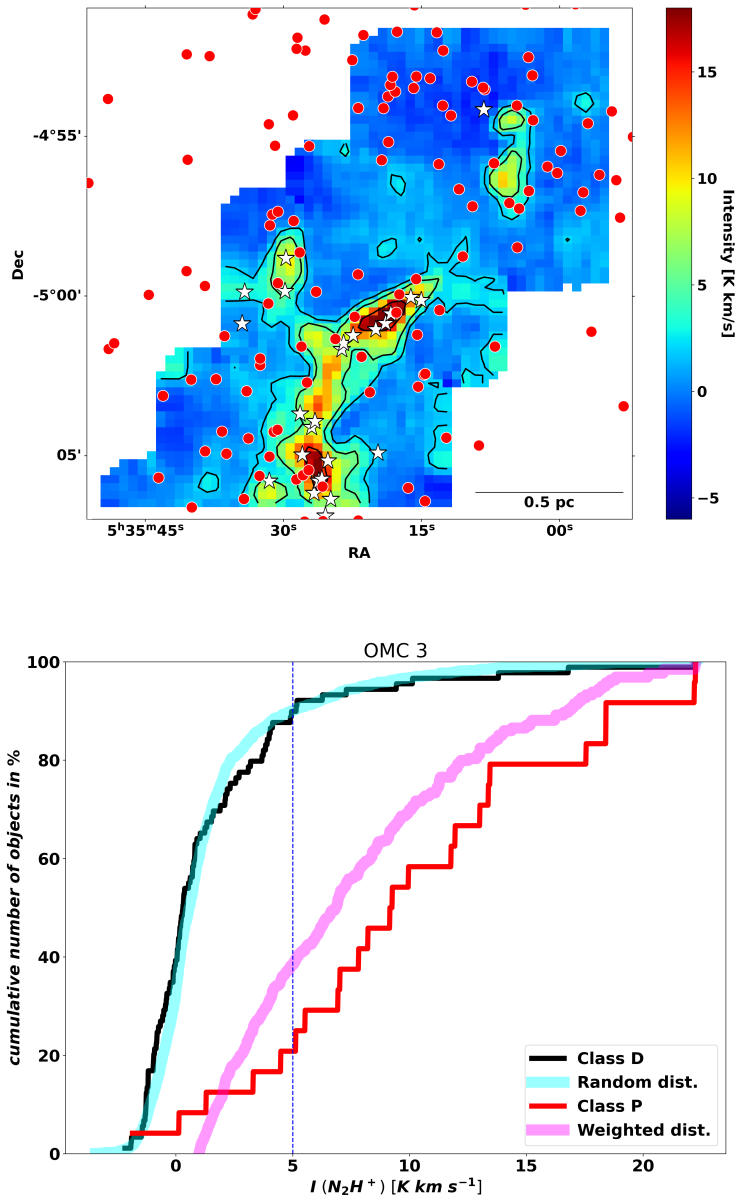

Figure 4.3: Top: *OMC 3* N_2H^+ intensity emission map (intensity level is colour coded in black), with positions of Class D objects (red dots) and Class P objects (white asterisk). Contour levels show 2, 5 and 15 [K km s^{-1}] N_2H^+ intensities. **Bottom**: The cumulative number of Class D (black line) and Class P objects (red line) as a function of N_2H^+ intensity. The cyan and magenta curves correspond to the cumulative proportion of objects resulting from the simulation (see 3.5) for the random distribution and the square-weighted distribution. The vertical blue dashed line corresponds to the 5 [K km s^{-1}] N_2H^+ intensity contour in the top plot.

4.2 ORION B

4.2.1 NGC 2023

NGC 2023 shows a similar distribution on the map (Figure 4.4) of both the Class P objects and the Class D objects. Both classes are found near higher densities, considered for this area . Class P objects are seen within the higher density structures, while the more developed Class D objects are seen in the periphery of the denser structures. The graph confirms this. The almost identical number of six Class P objects and eight Class D objects is noticeable. This results in $F_D = 1.3$. The SFR is at $\approx 3\ M_\odot$/Myr and the SFE is at $\approx 2\%$. 33% of Class D objects were found at values for $I(N_2H^+) > 5$ [K km s^{-1}]. This seems to be an area that is unfavourable for star formation.

4.2.2 NGC 2024

Looking at the map of the Flame Nebula or NGC 2024, on display in Figure 4.5, it shows a nearly perfect random distributed population of Class D objects. This is confirmed in the graphic. The shape of the simulated random distribution and the Class D objects largely overlap. The Class P objects also seem to be distributed rather randomly when looking at the map. Here too, the visual impression is confirmed by the graph. The Class P objects are found far from the square-weighted distribution towards lower densities and towards the simulated random distribution.

The value of the Class D objects fraction F_D is at a high level of 5.6 . The values found for the SFR is at $\approx 30\ M_\odot$/Myr and the SFE at $\approx 5\%$ are the highest ones which are found in the whole sample. Also in NGC 2024 the fraction is 33% of Class D objects at values for $I(N_2H^+) > 5$ [K km s^{-1}]. The massive stars found in this region, and their resulting feedback on the surroundings, produce this unique picture of a high SFR and a high SFE, with actual star formation correlating with less dense structures.

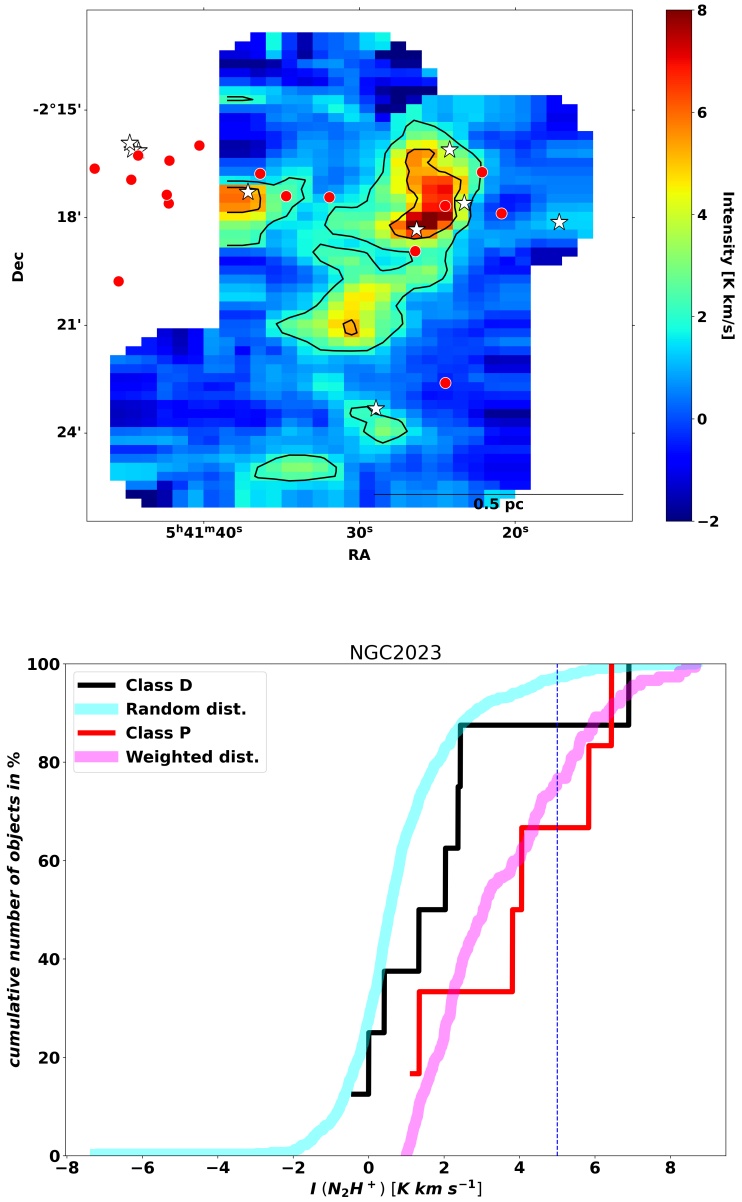

Figure 4.4: Top: *NGC 2023* N_2H^+ intensity emission map (intensity level is colour coded in black), with positions of Class D objects (red dots) and Class P objects (white asterisk). Contour level show 2 and 5 [K km s^{-1}] N_2H^+ intensity. **Bottom**: The cumulative number of Class D (black line) and Class P objects (red line) as a function of N_2H^+ intensity. The cyan and magenta curves correspond to the cumulative proportion of objects resulting from the simulation (see 3.5) for the random distribution and the square-weighted distribution. The vertical line corresponds to the 5 [K km s^{-1}] N_2H^+ intensity contour in the top plot.

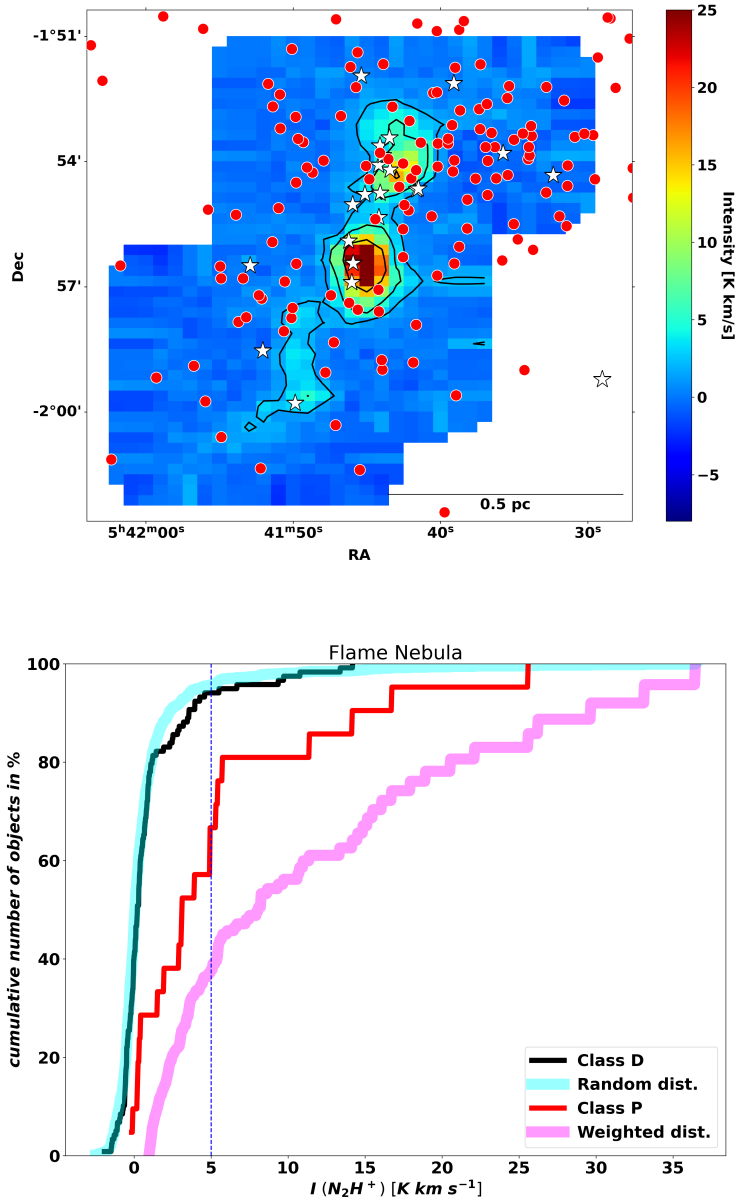

Figure 4.5: Top: *NGC 2024* N_2H^+ intensity emission map (intensity level is colour coded in black), with positions of Class D objects (red dots) and Class P objects (white asterisk). Contour levels show 2, 5 and 15 [K km s^{-1}] N_2H^+ intensities. **Bottom**: The cumulative number of Class D (black line) and Class P objects (red line) as a function of N_2H^+ intensity. The cyan and magenta curves correspond to the cumulative proportion of objects resulting from the simulation (see A.4) for the random distribution and the square-weighted distribution. The vertical line corresponds to the 5 [K km s^{-1}] N_2H^+ intensity contour in the top plot.

4.3 Evolutionary Parameters

The results obtained above show different characteristics of the relationship between dense gas and the respective Class P and Class D objects for each area. However, with the exception of NGC 2023, there is a clear separation of Class P and Class D objects, with Class P objects always observed at higher intensities in N_2H^+. This leads to the assumption that the Class P objects, whose most developed representatives are the Class Flat objects in this categorisation scheme, represent an upper limit for the age of the dense gas, which can be assumed to be ≈ 0.8 Myr according to Evans et al. (2009).

The catalogue of YSOs used in Hacar, Alves, et al. (2017) also includes Class Flat objects in the study of the relationship between protostars and dense gas in NGC 1333. The correlation with dense gas of the Class Flat objects deviates strongly from the Class I objects and largely follows the shape of Class II objects, which are the Class D objects in this study. Thus a lifetime of 0.5 Myr for the dense gas evolution can be assumed. In the regions with low gas densities investigated here, the more developed Class D objects are observed, with an age of ≈ 2 Myr (Evans et al., 2009). This means that dense gas structures have already been formed several times in this area and have also been depleted afterwards. This result is in good agreement with the argumentation in Hacar, Alves, et al. (2017).

4.4 Comparison with Previous Results

I would like to compare the previous results mentioned in 1.6 with the results found here. Starting with E. A. Lada (1992) their findings find agreement in this work. The star formation occurs almost solely within the dense ($n > 10^4$ cm^{-3}) gas is found by correlating Class P objects in the high N_2H^+ intensity regions, which together with the result that the N_2H^+(1-0) line is effectively generated at $n(H_2) > 10^4$ cm^{-3} leads to confirmation. Similarly, their finding that high gas densities and high gas masses may be necessary but not sufficient for star cluster formation, as some massive dense structures show low to no star formation activity, finds confirmation in Class P free regions of high density in LDN1641 N and OMC 3.

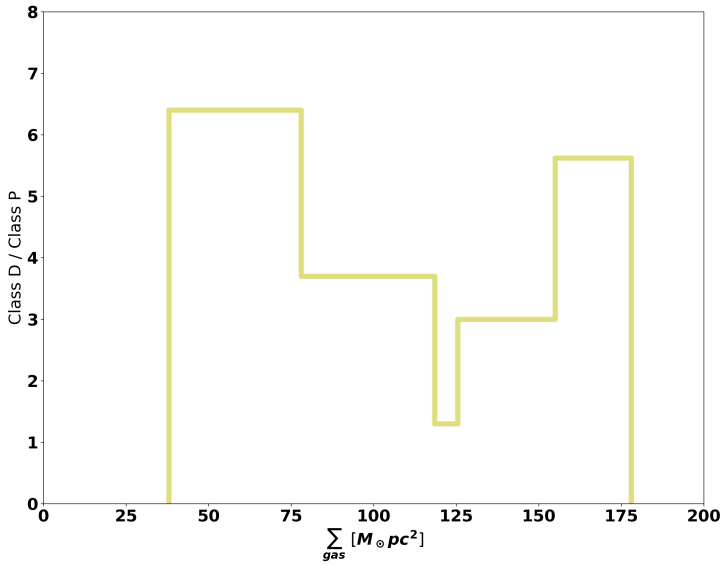

Figure 4.6: The Class D / Class P fraction vs mass relation found in this work. In Gutermuth et al. (2011) a continuous decrease in the ratio of class II to class I objects in relation to the gas column density is described for Orion. This observation is only confirmed for the areas with lower surface density. Higher values do not necessarily seem to produce a higher rate of youngest protostars relative to the more evolved population.

A decreasing Class II to Class I YSO ratio with increasing gas column density for the Orion cloud, within a common evolutionary state, representing only the embedded cloud population (defined by the YSO mass surface density versus the molecular gas mass column density squared), was presented by Gutermuth et al. (2011). Although the embedded cloud population represents more than the half of the population, it excludes the young protostar rich areas and the areas characterised by gas dispersal. Derived for the areas studied in this work, this result can only be confirmed for gas column density clusters up to $\sum_{gas}$ ≈120 $[M_\odot pc^{-2}]$. Because the area studied by Gutermuth et al. (2011) was the whole Orion cloud, as well as the limited population they presented in their relation, the comparison to the results discovered in this work should be taken with caution. In this work, the ratio of Class D to Class P objects has been investigated, that are consistent with the classification of YSOs in Gutermuth et al. (2011). Figure 4.6 presenting the result

shows the increasing ratio of Class D with respect to Class P objects at values above $\sum_{gas} > 120$ $[M_{\odot} pc^{-2}]$. It is possible that these areas of dense gas are inhibited in their ability to form protostars, as in the case of NGC 2024, where massive stars found in the area may cause this effect. But perhaps it is also a sign of the longevity and stability of very dense structures in the face of disturbances, which in turn prevent partly the formation of stars.

Last but not least, the comparison with the work of Hacar, Tafalla, and Alves (2017) which is particularly comparable, as the similar simulations were also made as here. The correlation found there in NGC 1333 between dense gas, which was also traced with $N_2H^+$and protostars is also evident in this work. The cumulative plot presented there can be compared most closely with the graph created here for OMC 3. It was also found there that, despite stellar feedback, dense gas can remain unaffected and trace the pristine gas structure of the young proto-cluster.

4.5 Areas by Comparison

Region	Mass $[M_{\odot}]$	Area [pc^2]	Class P	Class D	Class P$_{5K}$ [%]	F_D	SFR $[M_{\odot}/\mathrm{Myr}]$	SFE [%]
NGC 2024	193	1.08	21	118	33	5.6	27.8	5.2
NGC 2023	139	1.17	6	8	33	1.3	2.8	2.1
OMC 3	236	2	24	89	79	3.7	22.6	4.8
OMC 4	98	2.60	9	58	33	6.4	13.4	4.4
LDN1641 N	237	1.80	13	39	95	3.0	10.4	2.7

Table 4.1: The values for the investigated areas for the mass of dense molecular hydrogen, the area in pc^2, the number of Class P and Class D objects, the proportion of Class P objects with correlating intensity values I(N_2H^+) > 5 [K km s^{-1}] to their overall number, the ratio of Class D to Class P objects (F_D), also called the Class II / Class I ratio, the Star Formation Rate (Section 3.7) and the Star Formation Efficiency (Section 3.8).

With a look at table 4.1 you can see: The two areas that are similar in terms of data are OMC 3 and LDN1641 N. A high percentage, 79% for OMC 3 and even 95% for LDN1641 N, of the Class P objects are found at intensities above 5 [K km s^{-1}]. The SFE is with 4,8 % for OMC 3 nearly twice the value of 2.7 % for LDN1641 N, as well as the SFR with a value of 22.6 $M_{\odot}$/Myr for OMC 3 is more than double the value of 10.4 $M_{\odot}$/Myr for LDN1641 N. The ratio of Class D to Class P objects with 3.7 for OMC 3 and 3.0 for LDN1641 N are in a similar range. A current dynamic phase of star formation could be concluded for both areas.

Comparing Figure 4.3 and Figure 4.1, a stronger tendency of the Class D objects to random distribution can be seen for OMC 3, which could indicate a more intense earlier star formation phase, which took place in several regions of the area. Or the star formation started earlier, which is why the objects are more evenly distributed due to dynamic effects.

OMC 4 with 6.4 and NGC 2024 with 5.6 show similarities at the ratio of Class D to Class P objects. These are also the highest values determined for this parameter in this study. The values for Class P objects that are found at intensities above 5 [K km s^{-1}] are respectively 33%. The SFR of 27.8 $M_{\odot}$/Myr and an SFE of 5.2% for NGC 2024, the highest values in this sample, are significantly higher than for OMC 4. Here, the SFR is 13.4 $M_{\odot}$/Myr and the SFE is 4.4%. The curves of the Class D objects are almost congruent with the random distribution in Figure 4.2 and 4.5 . Together with the high ratio of Class D to Class P objects, these could be signs of an earlier violent star formation in both regions. In the more recent star formation, NGC 2024 seems to have the more intense phase, however, also has the much larger dense gas quantity at its disposal. The presence of massive stars in NGC 2024, and their influence on star formation, may contribute to the comparability of the current SFE.

NGC 2023, with a ratio of Class D to Class P objects of 1.3, has almost as many objects of each class. One could therefore speak of a very dynamic current star formation phase for this area. From the top part of Figure 4.4 one could deduce that some Class P objects arise in the same structures as the older Class D population. However, this could also be a projection effect.

Chapter 5

Conclusions

The gas properties of the component with a density of $n(H_2) \geq 10^4$ cm^{-3} in the Orion molecular cloud complex, LDN1641 N, OMC 4 and OMC 3 in the Orion A region and NGC 2023 and NGC 2024 in the Orion B region, were studied in relation to the YSOs of Class P and Class D that are found there. On the one hand, the study is based on IRAM 30m N_2H^+ (1-0) molecular line observations for tracing the dense gas. On the other hand, on the Catalogue of point sources and YSOs (Megeath et al., 2012). The YSOs have been used as indicators of star formation and as tracers of the formation and annihilation of dense molecular gas structures. The following results were achieved: Within the regions, a heterogeneous picture was obtained for the investigated parameters Star Formation Rate, Star Formation Efficiency and the fraction of Class D to Class P objects. The relation of dense gas ($n(H_2) \approx 10^5$ cm^{-3}) to the Class P and Class D objects also showed a different pattern in the different regions.

With the exception of NGC 2023, the younger Class P objects have always been found exclusively in regions of higher gas density.

The higher the column density, the higher the proportion of class D objects in relation to the younger Class P objects could only be found up to $\sum_{gas} \approx 120$ $[M_\odot pc^2]$.

In the LDN1641 N and OMC 3 areas, regions of higher density were found that do not correlate with any Class P objects, so dense gas structures are necessary but possibly not sufficient for star formation, unless star formation is in an early phase and cannot be observed with the methods used. The correlation of the younger

Class P objects and dense gas structures and the random distribution of the more evolved Class D objects suggests the dynamical creation and dispersion of dense molecular gas within a few lifetimes of the Class P objects. The upper limit for the age of dense gas structures is therefore in the range of ≈ 2 Myr, the mean lifespan of Class D objects.

5.1 Outlook

A combination of the available measurement results and catalogues with kinematic values for the motion of the protostars and the respective gas components would be an interesting addition to better understand the history and evolution of the proto-clusters. In order to determine the different conditions responsible for the heterogeneous image more precisely, further influencing factors such as magnetic fields, gravitational and turbulent influences as well as radiation in these areas should be included in the investigations.

Moreover, the structures and their formation on a wide range of scales, like hubs, filaments and fibres and their relationship with the areas under study should be investigated. Furthermore, it would be interesting to perform the same studies as done here, using a catalogue with a larger number of classes of protostars and pre-main sequence stars, and therefore higher resolution timescales of protostellar evolution.

Bibliography

Allen, L. E., & Davis, C. J. (2008). Low Mass Star Formation in the Lynds 1641 Molecular Cloud. In B. Reipurth (Ed.), *Handbook of star forming regions, volume i* (p. 621).

Andre, P., Ward-Thompson, D., & Barsony, M. (2000). From Prestellar Cores to Protostars: the Initial Conditions of Star Formation. In V. Mannings, A. P. Boss, & S. S. Russell (Eds.), *Protostars and planets iv* (p. 59).

Andre, P., Ward-Thompson, D., & Barsony, M. (1993). Submillimeter Continuum Observations of rho Ophiuchi A: The Candidate Protostar VLA 1623 and Prestellar Clumps. *Astrophysical Journal*, *406*, 122. https://doi.org/10.1086/172425

Astropy Collaboration, Price-Whelan, A. M., Lim, P. L., Earl, N., Starkman, N., Bradley, L., Shupe, D. L., Patil, A. A., Corrales, L., Brasseur, C. E., N"othe, M., Donath, A., Tollerud, E., Morris, B. M., Ginsburg, A., Vaher, E., Weaver, B. A., Tocknell, J., Jamieson, W., … Astropy Project Contributors. (2022). The Astropy Project: Sustaining and Growing a Community-oriented Open-source Project and the Latest Major Release (v5.0) of the Core Package. *apj*, *935*(2), Article 167, 167. https://doi.org/10.3847/1538-4357/ac7c74

Bally, J. (2008). Overview of the Orion Complex. In B. Reipurth (Ed.), *Handbook of star forming regions, volume i* (p. 459).

Bally, J., Langer, W. D., Stark, A. A., & Wilson, R. W. (1987). Filamentary Structure in the Orion Molecular Cloud. *Astrophysical Journal*, *312*, L45. https://doi.org/10.1086/184817

Beichman, C. A., Myers, P. C., Emerson, J. P., Harris, S., Mathieu, R., Benson, P. J., & Jennings, R. E. (1986). Candidate Solar-Type Protostars in Nearby

Molecular Cloud Cores. *Astrophysical Journal*, *307*, 337. https://doi.org/10.1086/164421

Bergin, E. A., & Tafalla, M. (2007). Cold Dark Clouds: The Initial Conditions for Star Formation. *Astronomy and Astrophysics Reviews*, *45*(1), 339–396. https://doi.org/10.1146/annurev.astro.45.071206.100404

Blaauw, A. (1964). The O Associations in the Solar Neighborhood. *Annual Review of Astron and Astrophys*, *2*, 213. https://doi.org/10.1146/annurev.aa.02.090164.001241

Blaauw, A. (1991). OB Associations and the Fossil Record of Star Formation. In C. J. Lada & N. D. Kylafis (Eds.), *The physics of star formation and early stellar evolution* (p. 125).

Bonnell, I. A., Bate, M. R., Clarke, C. J., & Pringle, J. E. (1997). Accretion and the stellar mass spectrum in small clusters. *Monthly Notices of the RAS*, *285*(1), 201–208. https://doi.org/10.1093/mnras/285.1.201

Briceno, C., Hartmann, L., Hernandez, J., Calvet, N., Vivas, A. K., Furesz, G., & Szentgyorgyi, A. (2007). 25 orionis: A kinematically distinct 10 myr old group in orion OB1a. *The Astrophysical Journal*, *661*(2), 1119–1128. https://doi.org/10.1086/513087

Briceño, C., Preibisch, T., Sherry, W. H., Mamajek, E. A., Mathieu, R. D., Walter, F. M., & Zinnecker, H. (2007). The Low-Mass Populations in OB Associations. In B. Reipurth, D. Jewitt, & K. Keil (Eds.), *Protostars and planets v* (p. 345).

Brown, A. G. A., de Geus, E. J., & de Zeeuw, P. T. (1994). The Orion OB1 association. I. Stellar content. *Astronomy and Astrophysics*, *289*, 101–120.

Burkert, A., & Hartmann, L. (2013). The Dependence of Star Formation Efficiency on Gas Surface Density. *Astrophysical Journal*, *773*(1), Article 48, 48. https://doi.org/10.1088/0004-637X/773/1/48

Caselli, P., Walmsley, C. M., Zucconi, A., Tafalla, M., Dore, L., & Myers, P. C. (2002). Molecular Ions in L1544. I. Kinematics. *Astrophysical Journal*, *565*(1), 331–343. https://doi.org/10.1086/324301

Chen, H., Tokunaga, A. T., & Fukui, Y. (1993). An IRAS Sample from Co-added Images of L1641. *Astrophysical Journal*, *416*, 235. https://doi.org/10.1086/173229

Comrie, A., Wang, K.-S., Hsu, S.-C., Moraghan, A., Harris, P., Pang, Q., Pińska, A., Chiang, C.-C., Simmonds, R., Chang, T.-H., Jan, H., & Lin, M.-Y. (2021). CARTA: Cube Analysis and Rendering Tool for Astronomy.

Contreras, Y., Garay, G., Rathborne, J. M., & Sanhueza, P. (2016). Fragmentation in filamentary molecular clouds. *Monthly Notices of the RAS*, *456*(2), 2041–2051. https://doi.org/10.1093/mnras/stv2796

di Francesco, J., Evans, I., N. J., Caselli, P., Myers, P. C., Shirley, Y., Aikawa, Y., & Tafalla, M. (2007). An Observational Perspective of Low-Mass Dense Cores I: Internal Physical and Chemical Properties. In B. Reipurth, D. Jewitt, & K. Keil (Eds.), *Protostars and planets v* (p. 17).

Dolan, C. J., & Mathieu, R. D. (2001). The Spatial Distribution of the λ Orionis Pre-Main-Sequence Population. *Astronomical Journal*, *121*(4), 2124–2147. https://doi.org/10.1086/319946

Enokiya, R., Ohama, A., Yamada, R., Sano, H., Fujita, S., Hayashi, K., Tsutsumi, D., Torii, K., Nishimura, A., Konishi, R., Yamamoto, H., Tachihara, K., Hasegawa, Y., Kimura, K., Ogawa, H., & Fukui, Y. (2021). High-mass star formation in Orion B triggered by cloud-cloud collision: Merging molecular clouds in NGC 2024. *Publications of the Astronomical Society of Japan*, *73*, S256–S272. https://doi.org/10.1093/pasj/psaa049

Evans, I., Neal J., Dunham, M. M., Jørgensen, J. K., Enoch, M. L., Merín, B., van Dishoeck, E. F., Alcalá, J. M., Myers, P. C., Stapelfeldt, K. R., Huard, T. L., Allen, L. E., Harvey, P. M., van Kempen, T., Blake, G. A., Koerner, D. W., Mundy, L. G., Padgett, D. L., & Sargent, A. I. (2009). The Spitzer c2d Legacy Results: Star-Formation Rates and Efficiencies; Evolution and Lifetimes. *Astrophysical Journal, Supplement*, *181*(2), 321–350. https://doi.org/10.1088/0067-0049/181/2/321

Greene, T. P., Wilking, B. A., Andre, P., Young, E. T., & Lada, C. J. (1994). Further Mid-Infrared Study of the rho Ophiuchi Cloud Young Stellar Population:

Luminosities and Masses of Pre–Main-Sequence Stars. *Astrophysical Journal*, *434*, 614. https://doi.org/10.1086/174763

Großschedl, J. E., Alves, J., Meingast, S., Ackerl, C., Ascenso, J., Bouy, H., Burkert, A., Forbrich, J., Fürnkranz, V., Goodman, A., Hacar, Á., Herbst-Kiss, G., Lada, C. J., Larreina, I., Leschinski, K., Lombardi, M., Moitinho, A., Mortimer, D., & Zari, E. (2018). 3D shape of Orion A from Gaia DR2. *Astronomy and Astrophysics*, *619*, Article A106, A106. https://doi.org/10.1051/0004-6361/201833901

Gutermuth, R. A., Pipher, J. L., Megeath, S. T., Myers, P. C., Allen, L. E., & Allen, T. S. (2011). A Correlation between Surface Densities of Young Stellar Objects and Gas in Eight Nearby Molecular Clouds. *Astrophysical Journal*, *739*(2), Article 84, 84. https://doi.org/10.1088/0004-637X/739/2/84

Hacar, A., Alves, J., Tafalla, M., & Goicoechea, J. R. (2017). Gravitational collapse of the OMC-1 region. *Astronomy and Astrophysics*, *602*, Article L2, L2. https://doi.org/10.1051/0004-6361/201730732

Hacar, A., Clark, S., Heitsch, F., Kainulainen, J., Panopoulou, G., Seifried, D., & Smith, R. (2022). Initial Conditions for Star Formation: A Physical Description of the Filamentary ISM. *arXiv e-prints*, Article arXiv:2203.09562, arXiv:2203.09562.

Hacar, A., Tafalla, M., & Alves, J. (2017). Fibers in the NGC 1333 proto-cluster. *aap*, *606*, Article A123, A123. https://doi.org/10.1051/0004-6361/201630348

Hacar, A., Tafalla, M., Forbrich, J., Alves, J., Meingast, S., Grossschedl, J., & Teixeira, P. S. (2018). An ALMA study of the Orion Integral Filament. I. Evidence for narrow fibers in a massive cloud. *Astronomy and Astrophysics*, *610*, Article A77, A77. https://doi.org/10.1051/0004-6361/201731894

Haro, G. (1953). Hα Emission Stars and Peculiar Objects in the Orion Nebula. *Astrophysical Journal*, *117*, 73. https://doi.org/10.1086/145669

Harvey, P. M., Thronson, J., H. A., & Gatley, I. (1980). A far-infrared study of the reflection nebula NGC 2023. *Astrophysical Journal*, *235*, 894–898. https://doi.org/10.1086/157692

Hertzsprung, E. (1905). Zur Stralung Der Strerne. *Zeitschrift Fur Wissenschaftliche Photographie*, *3*, 442–449.

Ishii, S., Nakamura, F., Shimajiri, Y., Kawabe, R., Tsukagoshi, T., Dobashi, K., & Shimoikura, T. (2019). Nobeyama 45 m mapping observations toward Orion A. II. Classification of cloud structures and variation of the ^{13}CO/C^{18}O abundance ratio due to far-UV radiation. *Publications of the Astronomical Society of Japan*, *71*, Article S9, S9. https://doi.org/10.1093/pasj/psz065

Jin, S., Song, L.-m., Zhang, Y.-P., & Zhang, H.-y. (2001). Molecular emission of ^{13}CO (J=1-0) and C ^{18}O (J=1-0) from OMC-3. *Chinese Astronomy and Astrophysics*, *25*(2), 170–180. https://doi.org/10.1016/S0275-1062(01)00058-3

Johnstone, D., & Bally, J. (1999). JCMT/SCUBA Submillimeter Wavelength Imaging of the Integral-shaped Filament in Orion. *Astrophysical Journal*, *510*(1), L49–L53. https://doi.org/10.1086/311792

Johnstone, D., & Bally, J. (2006). Large-Area Mapping at 850 μm. V. Analysis of the Clump Distribution in the Orion A South Molecular Cloud. *Astrophysical Journal*, *653*(1), 383–397. https://doi.org/10.1086/508852

Kirk, H., Myers, P. C., Bourke, T. L., Gutermuth, R. A., Hedden, A., & Wilson, G. W. (2013). Filamentary Accretion Flows in the Embedded Serpens South Protocluster. *Astrophysical Journal*, *766*(2), Article 115, 115. https://doi.org/10.1088/0004-637X/766/2/115

Lada, C. J., & Wilking, B. A. (1984). The nature of the embedded population in the rho Ophiuchi dark cloud : mid-infrared observations. *Astrophysical Journal*, *287*, 610–621. https://doi.org/10.1086/162719

Lada, C. J., & Lada, E. A. (1991). The nature, origin and evolution of embedded star clusters. In K. Janes (Ed.), *The formation and evolution of star clusters* (pp. 3–22).

Lada, C. J., & Lada, E. A. (2003). Embedded Clusters in Molecular Clouds. *Annual Review of Astron and Astrophys*, *41*, 57–115. https://doi.org/10.1146/annurev.astro.41.011802.094844

Lada, C. J., Muench, A. A., Luhman, K. L., Allen, L., Hartmann, L., Megeath, T., Myers, P., Fazio, G., Wood, K., Muzerolle, J., Rieke, G., Siegler, N., & Young, E. (2006). Spitzer Observations of IC 348: The Disk Population at 2-3 Million Years. *Astronomical Journal*, *131*(3), 1574–1607. https://doi.org/10.1086/499808

Lada, E. A. (1992). Global Star Formation in the L1630 Molecular Cloud. *Astrophysical Journal, Letters*, *393*, L25. https://doi.org/10.1086/186442

Lada, E. A., Evans, I., Neal J., & Falgarone, E. (1997). Physical Properties of Molecular Cloud Cores in L1630 and Implications for Star Formation. *Astrophysical Journal*, *488*(1), 286–306. https://doi.org/10.1086/304664

Larson, R. B. (1969). Numerical calculations of the dynamics of collapsing proto-star. *Monthly Notices of the RAS*, *145*, 271. https://doi.org/10.1093/mnras/145.3.271

Lombardi, M., Alves, J., & Lada, C. J. (2011). 2MASS wide field extinction maps. IV. The Orion, Monoceros R2, Rosette, and Canis Major star forming regions. *Astronomy and Astrophysics*, *535*, Article A16, A16. https://doi.org/10.1051/0004-6361/201116915

Megeath, S. T., Gutermuth, R., Muzerolle, J., Kryukova, E., Flaherty, K., Hora, J. L., Allen, L. E., Hartmann, L., Myers, P. C., Pipher, J. L., Stauffer, J., Young, E. T., & Fazio, G. G. (2012). THESURVEY OF THE ORION a AND b MOLECULAR CLOUDS. i. a CENSUS OF DUSTY YOUNG STELLAR OBJECTS AND a STUDY OF THEIR MID-INFRARED VARIABILITY. *The Astronomical Journal*, *144*(6), 192. https://doi.org/10.1088/0004-6256/144/6/192

Megeath, S. T., Gutermuth, R. A., & Kounkel, M. A. (2022). Low Mass Stars as Tracers of Star and Cluster Formation. *Publications of the ASP*, *134*(1034), Article 042001, 042001. https://doi.org/10.1088/1538-3873/ac4c9c

Meyer, M. R., Flaherty, K., Levine, J. L., Lada, E. A., Bowler, B. P., & Kandori, R. (2008). Star Formation in NGC 2023, NGC 2024, and Southern L1630. In B. Reipurth (Ed.), *Handbook of star forming regions, volume i* (p. 662).

Myers, P. C., & Ladd, E. F. (1993). Bolometric Temperatures of Young Stellar Objects. *Astrophysical Journal*, *413*, L47. https://doi.org/10.1086/186956

Ochsenbein, F., Bauer, P., & Marcout, J. (2000a). The VizieR database of astronomical catalogues. *Astrophysics and Space Science*, *143*, 23–32. https://doi.org/10.1051/aas:2000169

Ochsenbein, F., Bauer, P., & Marcout, J. (2000b). The VizieR database of astronomical catalogues. *Astrophysics and Space Science*, *143*, 23–32. https://doi.org/10.1051/aas:2000169

O'Dell, C. R., Muench, A., Smith, N., & Zapata, L. (2008). Star Formation in the Orion Nebula II: Gas, Dust, Proplyds and Outflows. In B. Reipurth (Ed.), *Handbook of star forming regions, volume i* (p. 544).

Palla, F., & Stahler, S. W. (1999). Star Formation in the Orion Nebula Cluster. *Astrophysical Journal*, *525*(2), 772–783. https://doi.org/10.1086/307928

Peterson, D. E., & Megeath, S. T. (2008). The Orion Molecular Cloud 2/3 and NGC 1977 Regions. In B. Reipurth (Ed.), *Handbook of star forming regions, volume i* (p. 590).

Pety, J., Guzmán, V. V., Orkisz, J. H., Liszt, H. S., Gerin, M., Bron, E., Bardeau, S., Goicoechea, J. R., Gratier, P., Le Petit, F., Levrier, F., Öberg, K. I., Roueff, E., & Sievers, A. (2017). The anatomy of the Orion B giant molecular cloud: A local template for studies of nearby galaxies. *Astronomy and Astrophysics*, *599*, Article A98, A98. https://doi.org/10.1051/0004-6361/201629862

Pokhrel, R., Myers, P. C., Dunham, M. M., Stephens, I. W., Sadavoy, S. I., Zhang, Q., Bourke, T. L., Tobin, J. J., Lee, K. I., Gutermuth, R. A., & Offner, S. S. R. (2018). Hierarchical Fragmentation in the Perseus Molecular Cloud: From the Cloud Scale to Protostellar Objects. *Astrophysical JournalAstrophysical Journal*, *853*(1), Article 5, 5. https://doi.org/10.3847/1538-4357/aaa240

Preibisch, T. (2012). The reliability of age measurements for young stellar objects from hertzsprung-russell or color-magnitude diagrams. *Research in Astronomy and Astrophysics*, *12*(1), 1–25. https://doi.org/10.1088/1674-4527/12/1/001

Racine, R. (1968). Stars in reflection nebulae. *Astronomical Journal*, *73*, 233–245. https://doi.org/10.1086/110624

Russell, H. N. (1914). Relations Between the Spectra and Other Characteristics of the Stars. *Popular Astronomy*, *22*, 275–294.

Shu, F. H., Adams, F. C., & Lizano, S. (1987). Star formation in molecular clouds: observation and theory. *Annual Review of Astron and Astrophys*, *25*, 23–81. https://doi.org/10.1146/annurev.aa.25.090187.000323

Skinner, S., Gagné, M., & Belzer, E. (2003). A Deep Chandra X-Ray Observation of the Embedded Young Cluster in NGC 2024. *Astrophysical Journal*, *598*(1), 375–391. https://doi.org/10.1086/378085

Stanke, T., Stutz, A. M., Tobin, J. J., Ali, B., Megeath, S. T., Krause, O., Linz, H., Allen, L., Bergin, E., Calvet, N., di Francesco, J., Fischer, W. J., Furlan, E., Hartmann, L., Henning, T., Manoj, P., Maret, S., Muzerolle, J., Myers, P. C., … Wilson, T. (2010). Hier ist wahrhaftig ein Loch im Himmel. The NGC 1999 dark globule is not a globule. *Astronomy and Astrophysics*, *518*, Article L94, L94. https://doi.org/10.1051/0004-6361/201014612

Stanke, T., Arce, H. G., Bally, J., Bergman, P., Carpenter, J., Davis, C. J., Dent, W., Di Francesco, J., Eislöffel, J., Froebrich, D., Ginsburg, A., Heyer, M., Johnstone, D., Mardones, D., McCaughrean, M. J., Megeath, S. T., Nakamura, F., Smith, M. D., Stutz, A., … Klein, T. (2022). The APEX Large CO Heterodyne Orion Legacy Survey (ALCOHOLS). I. Survey overview. *Astronomy and Astrophysics*, *658*, Article A178, A178. https://doi.org/10.1051/0004-6361/201937034

Strom, K. M., Strom, S. E., & Merrill, K. M. (1993). Infrared Luminosity Functions for the Young Stellar Population Associated with the L1641 Molecular Cloud. *Astrophysical Journal*, *412*, 233. https://doi.org/10.1086/172915

Takahashi, S., Ho, P. T. P., Teixeira, P. S., Zapata, L. A., & Su, Y.-N. (2013). Hierarchical Fragmentation of the Orion Molecular Filaments. *Astrophysical Journal*, *763*(1), Article 57, 57. https://doi.org/10.1088/0004-637X/763/1/57

Teixeira, P. S., Takahashi, S., Zapata, L. A., & Ho, P. T. P. (2016). Two-level hierarchical fragmentation in the northern filament of the Orion Molecular Cloud 1. *Astronomy and Astrophysics*, *587*, Article A47, A47. https://doi.org/10.1051/0004-6361/201526807

Van Rossum, G., & Drake, F. L. (2009). *Python 3 Reference Manual*. CreateSpace.

Walter, F. M., Sherry, W. H., Wolk, S. J., & Adams, N. R. (2008). The σ Orionis Cluster. In B. Reipurth (Ed.), *Handbook of star forming regions, volume i* (p. 732).

Ward-Thompson, D., André, P., Crutcher, R., Johnstone, D., Onishi, T., & Wilson, C. (2007). An Observational Perspective of Low-Mass Dense Cores II: Evolution Toward the Initial Mass Function. In B. Reipurth, D. Jewitt, & K. Keil (Eds.), *Protostars and planets v* (p. 33).

Weinreb, S., Barrett, A. H., Meeks, M. L., & Henry, J. C. (1963). Radio Observations of OH in the Interstellar Medium. *Nature*, *200*(4909), 829–831. https://doi.org/10.1038/200829a0

Williams, J. P., Blitz, L., & McKee, C. F. (2000). The Structure and Evolution of Molecular Clouds: from Clumps to Cores to the IMF. In V. Mannings, A. P. Boss, & S. S. Russell (Eds.), *Protostars and planets iv* (p. 97).

Wilson, B. A., Dame, T. M., Masheder, M. R. W., & Thaddeus, P. (2005). A uniform CO survey of the molecular clouds in Orion and Monoceros. *Astronomy and Astrophysics*, *430*, 523–539. https://doi.org/10.1051/0004-6361:20035943

Appendix A

Python Code

The Python programmes presented here are only equipped with the major steps. File handling and graphical representation routines have been partially omitted.

A.1 ZEROM

```
1
2  import glob
3  from astropy.utils.data import get_pkg_data_filename
4  from spectral_cube import SpectralCube
5  # assign directory
6  directory_Data = 'Data'
7  directory_Zero_moment = 'Zero'
8  # convert Jy to K
9  Jy_to_K = 0.156148264923739
10
11 # iterate over files in
12 # that directory
13 for filename in glob.iglob(f'{directory_Data}/*.fits'):
14     image_file = get_pkg_data_filename(filename)
15
16     # calculate zero moment using SpectralCube
17     cube = SpectralCube.read(image_file)
18     cube.spectral_slab(-5*u.m/u.s, 20*u.km/u.s) # integration range
19     m0 = cube.moment(order=0)
```

```
    m0 = m0 / 1000      # conversion for km/s
    m0 = m0 * Jy_to_K   #conversion for Jy to  K km/s

    # write zero moment fits file
    filename = filename.split("/")[-1]
    m0.write(directory_Zero_moment+filename,overwrite=True)
```

A.2 FITSCUT

```

from astropy import coordinates, units as u, wcs
from astropy.io import fits
from astropy.nddata.utils import Cutout2D
from astropy.wcs import WCS

# read in the FITS file with image data in the primary HDU
hdulist = fits.open('/path zo file')
hdu = hdulist[0]
header = hdulist[0].header
mywcs= wcs.WCS(hdu.header)
image_data = hdu.data

# perform the cutout with cutout 2d
# position of the cutout array center
coords = (X_coord,Y_coord)

# size of the cutout array along each axis
newsize = (X_size, Y_size)
cut = Cutout2D(image_data, position=coords, size=newsize, wcs = mywcs)
hdu.header.update(cut.wcs.to_header())
# IMPORTANT: to write out as fits file cut.data must be used
fits.writeto('/image path', cut.data , header,overwrite=True)
```

A.3 INYOUMAP

```
1
2  from astropy import coordinates, units as u, wcs
3  from astroquery.skyview import SkyView
4  from astroquery.vizier import Vizier
5  from astropy.io import fits
6  from matplotlib import pyplot
7  from pathlib import Path
8  import numpy as np
9  from mpl_toolkits.axes_grid1.anchored_artists import
       AnchoredDrawingArea
10 from matplotlib.patches import Circle
11 from mpl_toolkits.axes_grid1.anchored_artists import AnchoredSizeBar
12 from astropy.coordinates import SkyCoord
13 import matplotlib
14 import glob
15
16 # assign directory
17 directory_Data = 'path to zeromap files'
18
19 # iterate over files in
20 # that directory
21
22 for filename in glob.iglob(f'{directory_Data}/*'):
23     #select the object of interest for center coordinates
24     center_name = filename.split(".")[0]
25     center_name = center_name.split("/")[-1]
26     center = coordinates.SkyCoord.from_name(center_name)
27     hdulist = fits.open(filename)
28     hdu = hdulist[0]
29     plate_x_coord = hdulist[0].header['NAXIS1']
30     x_coord = np.linspace(0,plate_x_coord,plate_x_coord,endpoint =
       False)
31     plate_y_coord = hdulist[0].header['NAXIS2']
32     y_coord = np.linspace(0,plate_y_coord,plate_y_coord, endpoint =
       False)
```

```
33     center_plate_x_coord = plate_x_coord /2
34     center_plate_y_coord = plate_y_coord /2
35     mywcs = wcs.WCS(hdu.header)
36     center2 = coordinates.SkyCoord.from_pixel(center_plate_x_coord,
       center_plate_y_coord,mywcs, origin=0,mode='wcs')
37      # plot intensity map
38
39     fig = pl.figure(1,figsize=(16, 12), dpi=240)  #axis and legends
       fontstyle
40     font = {'family' : 'normal','weight' : 'bold','size'   : 20}
41     matplotlib.rc('font', **font)
42     fig.clf() # just in case one was open before
43     # use astropys wcsaxes tool to create an RA/Dec image
44     ax = fig.add_axes([0.15, 0.1, 0.8, 0.8], projection=mywcs)
45     ax.set_xlabel("RA",weight='bold')
46     ax.set_ylabel("Dec", weight='bold')
47     zero = ax.imshow(hdu.data[:,:] *0.156148264923739,vmin=-3, vmax=
       10, cmap= 'jet',aspect='auto')
48     intensity_bar = pyplot.colorbar(zero)
49     intensity_bar.set_label('Intensity [K km/s]', rotation=270, weight
       = 'bold', labelpad = 20)
50     levels =  [2,5,15] # np.linspace(-1,19,4)
51     pyplot.contour(x_coord, y_coord, hdu.data[:,:]*0.156148264923739,
       levels=levels,colors = 'black',linewidths = 2)
52     asb = AnchoredSizeBar(ax.transData,16,r"0.5 pc",loc='lower right',
       pad=0.1, borderpad=0.5, sep=5,framemeon=False)
53     ax.add_artist(asb)
54
55     # retrieve a specific table from Vizier to overplot with the
       protstars
56     Vizier.ROW_LIMIT = -1 # for unlimited results
57     tablelist = Vizier.query_region(center2, radius=20*u.arcmin,catalog
       ='J/AJ/144/192/table4',column_filters={'Cl': '==P'})
58     result=tablelist[0]
59     tbl_crds = coordinates.SkyCoord(result['RAJ2000'], result['DEJ2000'
       ],unit=(u.hour, u.deg), frame='fk5')
60
```

```
61     # query for overplot with the pre-main-sequence stars
62     tablelist2 = Vizier.query_region(center2, radius=20*u.arcmin,
       catalog='J/AJ/144/192/table4',column_filters={'Cl': '==D'})
63     result2=tablelist2[0]
64     tbl_crds2 = coordinates.SkyCoord(result2['RAJ2000'], result2['
       DEJ2000'],unit=(u.hour, u.deg), frame='fk5')
65
66     # overplot the data in the image
67     ax.plot(tbl_crds.ra, tbl_crds.dec, '*', markersize = 20,transform=
       ax.get_transform('fk5'), mec = 'black', mfc='white')
68     ax.plot(tbl_crds2.ra, tbl_crds2.dec,'o', markersize = 10,transform=
       ax.get_transform('fk5'), mec='white', mfc = 'red')
69
70     # zoom in on the relevant region to avoid whitespace
71     plate_x_coord = hdulist[0].header['NAXIS1']
72     plate_y_coord = hdulist[0].header['NAXIS2']
73     nans = np.isnan(hdu.data[:,:])#John Zwinck
74     nancols = np.all(nans, axis=0) #
75     nanrows = np.all(nans, axis=1) #
76     firstcol = nancols.argmin() #
77     firstrow = nanrows.argmin() #
78     lastcol = len(nancols) - nancols[::-1].argmin() #
79     lastrow = len(nanrows) - nanrows[::-1].argmin() #
80     ax.axis([firstcol, lastcol, firstrow, lastrow])
81     filename=filename.split(".")[0]
82     filename = filename.split("/")[-1]
83     # plot the intensity map with stars
84     pyplot.savefig('path to output folder/'+filename+'.png' )
```

A.4 COSITOM

```
1
2 # import required modules
3
4 from astropy import coordinates, units as u, wcs
5 from astroquery.vizier import Vizier
6 from astropy.io import fits
7 from astropy.coordinates import SkyCoord
8 from astropy.wcs.utils import skycoord_to_pixel
9 from statistics import mean
10 from scipy.stats import binned_statistic
11 import matplotlib.pyplot as plt
12 import numpy as np
13 from numpy import nan
14 from matplotlib.pyplot import figure
15 import glob
16
17 # assign directory
18 directory_Data = 'Zero_moment'
19 # initialize arrays for the Class P
20 # and Class D objects
21 P_Stars = []
22 D_Stars = []
23
24 # iterate over files in
25 # that directory
26 for filename in glob.iglob(f'{directory_Data}/*'):
27     #select the object of interest for center coordinates
28     hdulist = fits.open(filename)
29     hdu = hdulist[0]
30     plate_x_coord = hdulist[0].header['NAXIS1']
31     plate_y_coord = hdulist[0].header['NAXIS2']
32     center_plate_x_coord = plate_x_coord /2
33     center_plate_y_coord = plate_y_coord /2
34     mywcs = wcs.WCS(hdu.header)
35     center = coordinates.SkyCoord.from_pixel(center_plate_x_coord,
```

```
    center_plate_y_coord,mywcs, origin=0, mode='wcs')
36
37      # retrieve a specific table from Vizier to overplot
38      Vizier.ROW_LIMIT = -1 # for unlimited results
39      tablelist = Vizier.query_region(center, radius=20*u.arcmin,catalog=
    'J/AJ/144/192/table4',column_filters={'Cl': '==P'})
40      result=tablelist[0]
41      tbl_crds = coordinates.SkyCoord(result['RAJ2000'], result['DEJ2000'
    ],unit=(u.hour, u.deg), frame='fk5')
42
43      # a second overplot with the Class P objects
44      tablelist2 = Vizier.query_region(center, radius=20*u.arcmin,catalog
    ='J/AJ/144/192/table4',column_filters={'Cl': '==D'})
45      result2=tablelist2[0]
46      tbl_crds2 = coordinates.SkyCoord(result2['RAJ2000'], result2['
    DEJ2000'],unit=(u.hour, u.deg), frame='fk5')
47
48      # calculate pixelposition of found objects from skycoordinate
49      ref = SkyCoord(tbl_crds.ra, tbl_crds.dec, frame='fk5',unit=(u.
    hourangle, u.deg))
50      ref2 = SkyCoord(tbl_crds2.ra, tbl_crds2.dec, frame='fk5',unit=(u.
    hourangle, u.deg))
51      x_result,y_result = (skycoord_to_pixel(ref,mywcs,origin=0, mode='
    wcs'))
52      x2_result,y2_result = (skycoord_to_pixel(ref2,mywcs,origin=0, mode=
    'wcs'))
53
54      # find pixel values greater then array size
55      a = zip(x_result,y_result)
56      a = filter(lambda item: item[0] <= (plate_x_coord - 1)  and item[1]
     <= (plate_y_coord - 1), a)
57      a = filter(lambda item: item[0] >= 0 and item[1] >= 0, a)
58      x,y = map(list,zip(*a))
59      b = zip(x2_result,y2_result)
60      b = filter(lambda item: item[0] <= (plate_x_coord - 1) and item[1]
    <= (plate_y_coord - 1), b)
61      b = filter(lambda item: item[0] >= 0 and item[1] >= 0, b)
```

```
    x2,y2 = map(list,zip(*b))

    # coordinates to integer values
    xp = np.round(x)
    yp = np.round(y)
    xp = xp.astype(int)
    yp = yp.astype(int)

    xp2 = np.round(x2)
    yp2 = np.round(y2)
    xp2 = xp2.astype(int)
    yp2 = yp2.astype(int)

    #  Convert array to a list for simulation
    arr = hdu.data[:,:]
    arr = arr[~np.isnan(arr)]
    arr_quadratic_weight = (arr[arr>0])
    integer_arr_quadratic_weight = arr_quadratic_weight.astype(int)
    abs_integer_arr_quadratic_weight = np.absolute(
integer_arr_quadratic_weight)
    arr_quadratic_weight_sim  = arr_quadratic_weight.repeat(
abs_integer_arr_quadratic_weight)

    # get the intensity values at pixelpoint
    P_values =(hdu.data[yp,xp])
    P_values = [x for x in P_values if np.isnan(x) == False]
    P_values = np.array(P_values)
    D_values =(hdu.data[yp2,xp2])
    D_values = [x for x in D_values if np.isnan(x) == False]
    D_values = np.array(D_values)
    N_P=len(P_values)
    N_D=len(D_values)

    # for statistics the number of P and D objects
    print('N_P',N_P,'N_D',N_D, 'Fraction', N_P/(N_D)) # calculation of
the Class II  / Class I ratio

```

```
    # initialize the arrays for the simulation
    stat_D = []
    stat_P = []

    # statistic for the region and objects within
    I_sum_5 =np.sum(arr[arr>5])
    print ('sum array > 5K',I_sum_5, 'Number of pixels with value > 5K'
    ,len(arr[arr>5]))
    I_sum = np.sum (arr[arr > 0 ])
    print ('sum array > 0K', I_sum,'Number of pixels with value > 0K',
    len(arr[arr > 0]))
    I_sum_all = np.sum (arr)
    print ('sum array all', I_sum_all,'Number of pixels all',len(arr))
    SFR = N_D / 4
    print('SFR',SFR)
    N_sum_5 = ((7.9 * I_sum_5) + 8.2 ) * 1e21
    print ('N(H) > 5K =', N_sum_5)
    N_sum = ((7.9 * I_sum) + 8.2 ) * 1e21
    print ('N(H) > 0K =', N_sum)
    N_sum_all = ((7.9 * I_sum_all) + 8.2 ) * 1e21
    print ('N(H) all =', N_sum_all)

    area = (0.00098 * len (arr))
    area_0 = (0.00098 * len (arr[arr > 0]))
    area_5 = (0.00098 * len (arr[arr > 5]))
    print ('area = ', area,'pc²' )
    print ('area > 0K = ', area_0,'pc²' )
    print ('area > 5K = ', area_5,'pc²' )

# simulation:
# number of object in region are distributed over the measured
 intensities
# within the region
    import random
    np.random.seed(555)
    for i in range(0,1000):

```

```
130         rand_D = np.random.choice(arr, N_D)
131         stat_D = np.append(stat_D, rand_D)
132         rand_P = np.random.choice(arr_quadratic_weight_sim, N_P)
133         stat_P = np.append(stat_P,rand_P)
134 
135     # convert data for cumulative presentation
136     result_D, bin_result_D = np.histogram(D_values, bins = len(arr))
137     stat_histo_D , bin_stat_D = np.histogram(stat_D, bins = len(arr))
138     result_P, bin_result_P = np.histogram(P_values, bins = len(arr))
139     stat_histo_P , bin_stat_P = np.histogram(stat_P, bins = len(arr))
```